Available online at www.sciencedirect.com
ScienceDirect
Journal of Computational Physics 227 (2008) 4089–4122
JOURNAL OF COMPUTATIONAL PHYSICS
www.elsevier.com/locate/jcp

Wavenumber-extended high-order oscillation control finite volume schemes for multi-dimensional aeroacoustic computations

Sungtae Kim, Soogab Lee, Kyu Hong Kim *

School of Mechanical and Aerospace Engineering and the Institute of Advanced Aerospace Technology, Seoul National University, Seoul 151-742, South Korea

Received 12 February 2007; received in revised form 13 December 2007; accepted 14 December 2007
Available online 28 December 2007

Abstract

A new numerical method toward accurate and efficient aeroacoustic computations of multi-dimensional compressible flows has been developed. The core idea of the developed scheme is to unite the advantages of the wavenumber-extended optimized scheme and M-AUSMPW+/MLP schemes by predicting a physical distribution of flow variables more accurately in multi-space dimensions. The wavenumber-extended optimization procedure for the finite volume approach based on the conservative requirement is newly proposed for accuracy enhancement, which is required to capture the acoustic portion of the solution in the smooth region. Furthermore, the new distinguishing mechanism which is based on the Gibbs phenomenon in discontinuity, between continuous and discontinuous regions is introduced to eliminate the excessive numerical dissipation in the continuous region by the restricted application of MLP according to the decision of the distinguishing function. To investigate the effectiveness of the developed method, a sequence of benchmark simulations such as spherical wave propagation, nonlinear wave propagation, shock tube problem and vortex preservation test problem are executed. Also, throughout more realistic shock–vortex interaction and muzzle blast flow problems, the utility of the new method for aeroacoustic applications is verified by comparing with the previous numerical or experimental results.

Keywords: Computational aeroacoustics; Dispersion relation; Wavenumber-extended optimization; M-AUSMPW+; MLP; Shock–vortex interaction; Muzzle blast flow

1. Introduction

The analysis of more complex flow physics has been required continually with the development of the aerospace industry. Recent requirements have focused on the utility of computational aeroacoustics (CAA) and have extended its applications widely [1,2]. Recently, there has been much attention on complex nonlinear

* Corresponding author. Tel.: +82 2 880 9346; fax: +82 2 887 2662.
E-mail address: aerocfd1@snu.ac.kr (K.H. Kim).

0021-9991/$ - see front matter © 2007 Elsevier Inc. All rights reserved.
doi:10.1016/j.jcp.2007.12.013

phenomena beyond simple linear physics, such as vortex dynamics and shock–vortex interaction, jet screech and shock-associated jet noise, cavity noise, gun-firing muzzle blast noise and blade–vortex interaction. [3,4]. Generally, many of these nonlinear phenomena are related to a shock or discontinuity, and its interaction with a sound field makes the problem more complex. Therefore, higher computational cost and data storage have been required for numerical simulations. Furthermore, the stable handling of such a discontinuity has been one of the most important issues not only in CAA but also in Computational Fluid Dynamics (CFD). Because most of CFD and CAA are based on continuous functions, it is essentially impossible to deal with a discontinuity perfectly. In order to overcome this defect, a discontinuity is designed to be captured with a kind of tricks, i.e., by introducing the intermediate state within a numerical shock region, which is far from physical phenomena. This improper unphysical state may lead to spurious oscillations and instability around a discontinuity. At present, shock can be captured stably by removing these oscillations. However, the decrease in the order of spatial accuracy is unavoidable because of the introduction of some dissipation in the local region of the shock. It is a very serious problem in CAA because the capturing of sound generation essentially necessitates a higher-order accurate scheme with low artificial dissipation compared to a conventional CFD requirement. Thus, in order to solve acoustic problems including a discontinuity, the numerical scheme should be chosen or developed in consideration of the contrary aspect mentioned above. We claim that *the numerical schemes for CAA must have higher-order spatial accuracy combined with a very sophisticated oscillation control mechanism*.

Firstly, concerning high-order and high-resolution schemes for the CAA, there have been compact schemes [5], DRP (dispersion-relation preserving) schemes [6] and wavenumber-extended finite difference schemes [7] which optimize the scheme coefficients to minimize a particular type of error instead of the truncation error. Successively, a variety of optimized schemes [7–12] have been designed to resolve acoustic solutions more accurately. However, central difference schemes, of which the form most optimized schemes have, may provide spurious solutions, which may lead to inevitable stability problems that must be treated by the use of filters or explicit dissipation terms [11–13]. The required amount of artificial dissipation is problem-dependent, and one may need to perform laborious numerical tests to obtain the best result for a particular problem. Although several researchers developed upwind optimized schemes [7,13–15] to improve the quality of the high wavenumber solution without adding an explicit artificial damping terms, they could not eliminate the spurious numerical oscillations perfectly. In worse cases, additional artificial dissipation or filtering is also needed to damp them out.

Secondly, as for the oscillation control schemes, numerous studies have been carried out since the late 1970s and several important concepts, such as TVD, TVB and ENO, have been proposed for better convergence and stable calculation. The concept of TVD (Total Variation Diminishing) was proven to be extremely successful in solving hyperbolic conservation laws [16,17]. Although the TVD criterion provides a fundamental idea for oscillation control and is still very popular, conventional TVD schemes yield somewhat unsatisfactory results near extrema in terms of accuracy and convergence. In order to overcome this limitation, ENO (essentially non-oscillatory) schemes [18] and the concept of TVB (total variation bounded) [19] were introduced. Although ENO or WENO (weighted essentially non-oscillatory) [20] avoids unphysical clipping at extrema and enhances accuracy, it may yield an undershoot and/or overshoot in multi-space dimensions, which may influence the convergence badly because its oscillation control capability is proven only in one-dimensional scalar equation. For that reason, the multi-dimensional limiting process (MLP) [21] was developed as an oscillation control method in multi-dimensional applications. By the help of a multi-dimensional limiting function, MLP shows robust convergence and higher spatial accuracy. As a result, it yields very desirable properties in terms of accuracy, efficiency and robustness compared with other higher-order interpolation schemes such as ENO/WENO.

In summary of the characteristics mentioned above, the numerical scheme which is suitable for CAA requires the followings:

(*r*1) *For the accurate and stable evaluation of the propagation of acoustic waves, the numerical scheme should automatically have proper dissipation and low dispersion characteristics in a non-discontinuous region.*

(*r*2) *For monotonic behavior across a multi-dimensional discontinuity, the numerical scheme should have an appropriate oscillation control capability without loss of accuracy in a non-discontinuous region.*

The major purpose of the present paper is to develop the new schemes which satisfy the above characteristics for the accurate and robust aeroacoustic calculation with discontinuity. With respect to the requirement (1), M-AUSMPW+ [22] is considered as one of the solutions. In M-AUSMPW+, the characteristics of the central scheme and upwind scheme are switched properly and automatically based on the flow condition. As a result, M-AUSMPW+ produces proper numerical dissipation according to the flow situation. In the smooth region where little dissipation is necessary, M-AUSMPW+ has the characteristic of the central scheme and minimizes the numerical dissipation. On the other hand, in the rapidly varying region or supersonic region, it has the characteristic of the upwind scheme. Thus, numerical instability can be restricted automatically. Ref. [22] is, however, focused just on the development of the higher-order upwind scheme and the reduction of dissipation, i.e., M-AUSMPW+ has been designed without consideration of the propagation of acoustic waves, which induces some dispersion problems. *As a result, the first objective is to develop the wavenumber-extended optimized schemes for finite volume approaches and to combine the advantages of both the developed schemes and M-AUSMPW+.*

With respect to requirement (2), MLP is thought to be the best solution for multi-dimensional discontinuity. However, in the continuous region, MLP, similar to most previous limiters, has a tendency to damp out the amplitude of linear acoustic waves seriously. *Therefore, the second objective is to introduce a new distinguishing mechanism between the continuous and the discontinuous regions and to combine it with MLP to eliminate the excessive dissipation in the continuous region.*

The developed scheme is tested by solving several benchmark problems presented by the Institute for Computer Application in Science and Engineering/NASA Langley Research Center (ICASE/LaRC) workshop on CAA [23], and so on. In addition, two-dimensional flow fields produced by shock–vortex interactions and by a supersonic-discharging projectile from a shock tube are simulated numerically. The numerical results are compared with solutions computed by other numerical schemes and with exact solutions or experimental results.

The outline of the remainder of this article is as follows. First, the key ideas of the present work are briefly provided in Section 2. The method to treat the continuous region, which couples with M-AUSMPW+ and the conservative wavenumber-extended optimization technique for finite volume approaches, is explained in Section 3, and the oscillation control method is introduced with an emphasis on the newly developed distinguishing mechanism in Section 4. In Section 5, the developed scheme is applied to a number of benchmark test cases and two more realistic problems, i.e., the sound generation of shock–vortex interaction and the muzzle blast flow problem. Then the conclusion of this work is drawn in Section 6.

2. Key ideas

One of the challenges in CAA is the development of a new scheme to reduce excessive numerical dispersion and dissipation while numerical oscillations are prevented across multi-dimensional discontinuity. In order to cope with the requirements, a numerical scheme should be able to reflect the proper flow phenomena. However, up to now, most successful numerical methods, including spatial discretization and interpolation schemes, have been developed based on one-dimensional flow physics and proven only in one-dimensional scalar wave equation. Because a system of multi-dimensional governing equations, i.e., multi-dimensional Euler or Navier–Stokes equations, support more various flow phenomena such as multi-dimensional contact discontinuity, oblique shock, expansion fan and vortex flow, a straightforward extension of the scheme, which is based on one-dimensional flow physics, to multi-dimensional flows may lead to insufficient or excessive numerical dissipation. In order to incorporate multi-dimensional physical phenomena, a numerical scheme should be able to adjust the numerical dissipation properly in accordance with various multi-dimensional physical situations. Furthermore, different from mathematics, a continuous function in computation can no longer maintain the characteristics of it as the number of mesh points decreases. That is, if the number of mesh points is too small to express the continuous function, it would appear to be some kind of discontinuity, which may lead to the stability problem again and thus, require proper numerical dissipation.

With regard to this issue, the key idea of the new method is to modify the amount of numerical dissipation by considering flow physics, which is categorized into three types: smooth region, rapidly varying region, and discontinuity. In the present work, the continuous region is divided into the smooth region and the rapidly varying

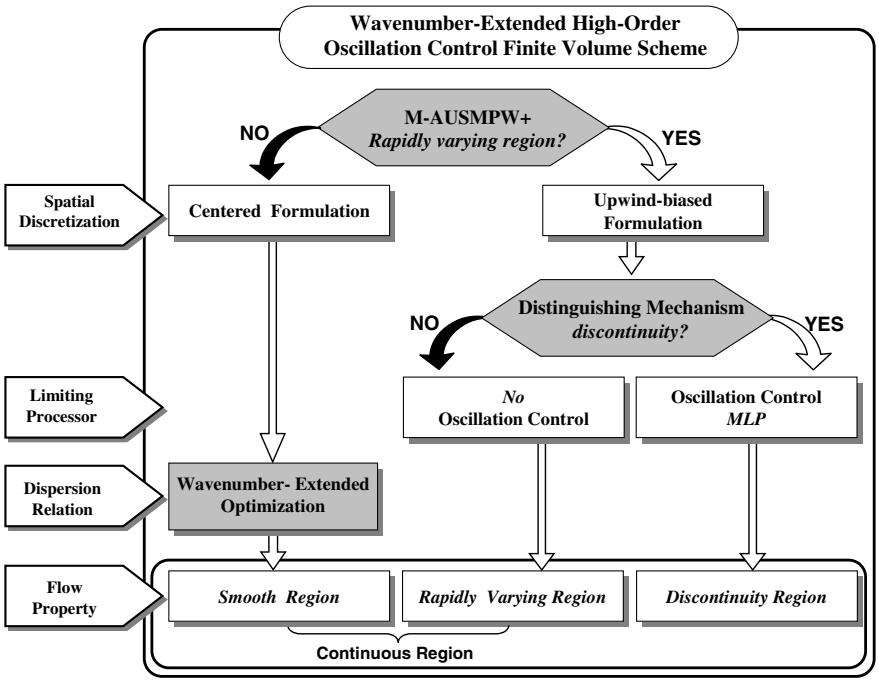

Fig. 1. Schematic diagram of the wavenumber-extended high-order finite volume scheme.

region. Through the use of M-AUSMPW+ as the baseline scheme, the developed scheme can distinguish the smooth region from the rapidly varying region automatically. In the smooth region, the characteristic of the spatial discretization is switched automatically into that of the newly proposed wavenumber-extended centered finite volume scheme in order to minimize the numerical dispersion errors while no dissipation errors are produced essentially. In the rapidly varying region including the discontinuous region, on the other hand, the developed scheme has the characteristics of the upwind-biased scheme so the artificial dissipation is determined properly. In addition, by the newly introduced distinguishing mechanism, the developed scheme differentiates the discontinuous region from the continuous region which consists of the smooth region and the rapidly varying region. After that, only in the discontinuous region, a multi-dimensional oscillation control scheme (MLP) is applied to provide non-oscillatory profiles without compromising the accuracy in the non-discontinuous region. Fig. 1 summarizes the schematic of the developed scheme.

Based on the category defined above, the wavenumber-extended optimization technique and MLP are properly applied to each region. The procedure of optimization is similar to that proposed in Ref. [24] to derive the low-dispersion finite volume (LDFV) scheme. However, the following features have been improved. Firstly, the developed wavenumber-extended optimization technique considers the minimization of the dispersion error in the smooth region and the minimization of the dissipation error in the rapidly varying region simultaneously. Secondly, it is based on the conservative requirement of reconstruction from cell averages rather than a non-conservative one, which is appropriate for finite volume approaches.

3. Method to treat continuous region

In the present work, the continuous region consists of the smooth region and the rapidly varying region. To handle the continuous region accurately, we chose M-AUSMPW+ as the spatial discretization scheme. The core idea of M-AUSMPW+ is to re-evaluate the convective quantity at cell-interface by considering flow physics. Through the analysis of TVD limiters, simple criterion between the smooth region and the rapidly varying region is proposed, and the convective quantity is re-evaluated according to the criterion, which can eliminate the numerical dissipation effectively in non-flow aligned grid system. As a result, the new

treatment of convective flux substantially improves the solution in the smooth region without compromising the accuracy in the rapidly varying region or the discontinuous region.

However, direct applications of the form of Ref. [22] for CAA may lead to the dispersion problem because Ref. [22] is designed for high resolution of discontinuities and high formal order of accuracy, and not for acoustic waves. Even though schemes with higher formal order of accuracy give more accurate result for the best-resolved wave component, it is well known that the truncation error analysis only is insufficient to examine the dispersion errors of the schemes. Therefore, by introducing additional constraints concerning the dispersion errors through the Fourier analysis, we developed conservative wavenumber-extended high-order interpolations for the finite volume approach, which are intended to solve the acoustic portion of the solution accurately, in conjunction with M-AUSMPW+.

3.1. Fourier analysis of finite volume schemes

In order to develop the conservative wavenumber-extended high-order interpolations, the following reconstruction from cell averages with a conservative approximation has to be considered first [25].

Suppose the interpolation is carried out in a scaled coordinate ξ, where the grid-point spacing $\Delta\xi$ is uniform. Given a scaled grid

$$a = \xi_{\frac{1}{2}} < \xi_{\frac{3}{2}} < \cdots < \xi_{N-\frac{1}{2}} < \xi_{N+\frac{1}{2}} = b, \tag{3.1}$$

cells, cell centers, and cell sizes can be defined as

$$I_i \equiv \left[\xi_{i-\frac{1}{2}}, \xi_{i+\frac{1}{2}}\right], \quad \xi_i \equiv \frac{1}{2}\left(\xi_{i-\frac{1}{2}} + \xi_{i+\frac{1}{2}}\right), \ \ i = 1, 2, \ldots, N. \tag{3.2}$$

The cell average values of a function $\varphi(\xi)$ for each cell I_i are defined as

$$\bar{\varphi}_i \equiv \frac{1}{\Delta\xi_i}\int_{\xi_{i-\frac{1}{2}}}^{\xi_{i+\frac{1}{2}}} \varphi(\xi)\mathrm{d}\xi, \quad i = 1, 2, \ldots, N. \tag{3.3}$$

Given the location I_i and the order of accuracy k, a candidate stencil $S(i)$, based on $r$cells to the left, s cells to the right, and I_i itself if $r,s \geqslant 0$, can be chosen with $r + s + 1 = k$:

$$S(i) \equiv \{I_{i-r}, \ldots, I_{i+s}\}. \tag{3.4}$$

Then, we can find a unique polynomial $p_i(\xi)$ of degree at most $k - 1 = r + s$, which is a kth order accurate approximation to the function $\varphi(\xi)$ inside I_i:

$$p_i(\xi) = \varphi(\xi) + \mathrm{O}(\Delta\xi^k), \quad \xi \in I_i, \ \ i = 1, 2, \ldots, N. \tag{3.5}$$

And the cell average of $p_i(\xi)$ in each of the cells in $S(i)$ agrees with that of $\varphi(\xi)$:

$$\frac{1}{\Delta\xi_j}\int_{\xi_{j-\frac{1}{2}}}^{\xi_{j+\frac{1}{2}}} p_i(\xi)\mathrm{d}\xi = \bar{\varphi}_j, \quad j = i - r, \ldots, i + s. \tag{3.6}$$

This gives approximations to the function $\varphi(\xi)$ at two cell interfaces of cell i,

$$\varphi^-_{i+\frac{1}{2}} = \varphi\left(\xi_{i+\frac{1}{2}}\right) + \mathrm{O}(\Delta\xi^k), \quad \varphi^+_{i-\frac{1}{2}} = \varphi\left(\xi_{i-\frac{1}{2}}\right) + \mathrm{O}(\Delta\xi^k), \ \ i = 1, 2, \ldots, N. \tag{3.7}$$

Since the approximation from the given cell averages $\bar{\varphi}_j$ in the stencil $S(i)$ to the values $\varphi^-_{i+\frac{1}{2}}$ and $\varphi^+_{i-\frac{1}{2}}$ in Eq. (3.5) are linear, we can find constants c_{rj} and $\tilde{c}_{rj}$, which depend on the left shift of stencil r of the stencil $S(i)$, on the order of accuracy k and on the cell sizes $\Delta\xi_j$, such that

$$\varphi^-_{i+\frac{1}{2}} = \sum_{j=0}^{k-1} c_{rj}\bar{\varphi}_{i-r+j}, \quad \varphi^+_{i-\frac{1}{2}} = \sum_{j=0}^{k-1} \tilde{c}_{rj}\bar{\varphi}_{i-r+j}. \tag{3.8}$$

If we identify the left shift r not with the cell I_i but with the point of reconstruction $\xi_{i+\frac{1}{2}}$, then it is clear that

$$\tilde{c}_{rj} = c_{r-1,j}. \tag{3.9}$$

From now on, let us discuss the Fourier analysis for dispersion characteristics. In a high-order finite volume scheme, the flow quantities at a cell-interface is obtained from a high-order polynomial interpolation formula. Suppose we use the above conservative approximation in stencil $S(i)$ for φ, and with C_{rj} constants say,

$$\varphi_{i+\frac{1}{2}} = \sum_{j=0}^{k-1} C_{rj}\bar{\varphi}_{i-r+j}. \tag{3.10}$$

From Eq. (3.10),

$$\begin{aligned}\varphi\left(\xi_i + \frac{1}{2}\Delta\xi\right) &= \sum_{j=0}^{k-1} C_{rj}\bar{\varphi}(\xi_i + (j-r)\Delta\xi) = \sum_{j=0}^{k-1} C_{rj}\cdot\frac{1}{\Delta\xi}\int_{\xi_i+(j-r)\Delta\xi-\frac{1}{2}\Delta\xi}^{\xi_i+(j-r)\Delta\xi+\frac{1}{2}\Delta\xi}\varphi(\zeta)\mathrm{d}\zeta \\ &= \sum_{j=0}^{k-1} C_{rj}\cdot\frac{1}{\Delta\xi}\left[\int_0^{\xi_i+(j-r)\Delta\xi+\frac{1}{2}\Delta\xi}\varphi(\zeta)\mathrm{d}\zeta - \int_0^{\xi_i+(j-r)\Delta\xi-\frac{1}{2}\Delta\xi}\varphi(\zeta)\mathrm{d}\zeta\right].\end{aligned} \tag{3.11}$$

By applying the Fourier transform to Eq. (3.11) with ξ_i as the variable of integration and using the Derivative, Shifting and Integration theorems, it is found

$$\tilde{\varphi}(\alpha\Delta\xi)\cdot \mathrm{e}^{\sqrt{-1}\alpha\frac{1}{2}\Delta\xi} = \tilde{\varphi}(\alpha\Delta\xi)\cdot\sum_{j=0}^{k-1} C_{rj}\frac{1}{\Delta\xi}\left[\frac{1}{\sqrt{-1}\alpha}\mathrm{e}^{\sqrt{-1}\alpha\left(j-r+\frac{1}{2}\right)\Delta\xi} - \frac{1}{\sqrt{-1}\alpha}\mathrm{e}^{\sqrt{-1}\alpha\left(j-r-\frac{1}{2}\right)\Delta\xi}\right], \tag{3.12}$$

where $\tilde{\varphi}$ is the Fourier transform pair of φ.

Therefore, we can define the effective wavenumber of the finite volume scheme as follows:

$$\bar{\alpha} \equiv \frac{-\sqrt{-1}}{\Delta\xi}\sum_{j=0}^{k-1} C_{rj}(\mathrm{e}^{\sqrt{-1}\alpha(j-r)\Delta\xi} - \mathrm{e}^{\sqrt{-1}\alpha(j-r-1)\Delta\xi}). \tag{3.13}$$

In general, the modified wavenumber $k^* \equiv \bar{\alpha}\Delta\xi$ is a periodic complex function of $k \equiv \alpha\Delta\xi$ with a period of 2π. The real part k_r^* and the imaginary part k_i^* are associated with the dispersion error (phase error) and the dissipation error (amplitude error), respectively, [7,26].

$$\begin{aligned} k_r^* &\equiv \bar{\alpha}_r\Delta\xi = \sum_{j=0}^{r+s} C_{rj}(\sin[(j-r)k] - \sin[(j-r-1)k]), \\ k_i^* &\equiv \bar{\alpha}_i\Delta\xi = \sum_{j=0}^{r+s} C_{rj}(\cos[(j-r-1)k] - \cos[(j-r)k]). \end{aligned} \tag{3.14}$$

To assure that the Fourier transform of the finite volume schemes is a good approximation to the physical state of the flow quantity, it is required that the coefficients c_{rj} be chosen to minimize the integrated error, E_r, for a particular wavenumber range of $0 \leqslant \alpha\Delta\xi \leqslant \eta$, where,

$$E_r = \int_0^{\eta}\{\lambda[k_r^* - \alpha\Delta\xi]^2 + (1-\lambda)[k_i^*]^2\}\mathrm{d}k, \tag{3.15}$$

and λ is the balancing coefficient for the real and imaginary (i.e., numerical dispersion and dissipation error), respectively.

3.2. Baseline scheme: M-AUSMPW+

The convective flux of AUSM-type schemes is written as follows:

$$\mathbf{F}_{\frac{1}{2}} = m_{\frac{1}{2}}c_{\frac{1}{2}}\mathbf{\Phi}_{L \text{ or } R}, \tag{3.16}$$

where $m_{\frac{1}{2}}$ is the cell-interface Mach number and $\mathbf{\Phi}$ is the transferred quantity vector. In M-AUSMPW+, the flux form of Eq. (3.16) changes to Eq. (3.17) to reflect the difference between the rapidly varying region and the smooth region more clearly:

$$\mathbf{F}_{\frac{1}{2}} = m_{\frac{1}{2}} c_{\frac{1}{2}} \mathbf{\Phi}_{L \text{ or } R,\frac{1}{2}}, \tag{3.17}$$

where $\mathbf{\Phi}_{L,R,\frac{1}{2}}$ is the modified convective quantity in a cell-interface.

Simply stated, the fundamental difference from previous AUSM-type schemes is the appropriate modification of the convective quantity at a cell-interface in the rapidly varying region and the smooth region.

Generally, cell-interface quantities are prepared as

$$\mathbf{\Phi}_L = \overline{\mathbf{\Phi}}_i + 0.5\Delta\mathbf{\Phi}|_i = \overline{\mathbf{\Phi}}_i + 0.5\phi(r_L)\Delta\mathbf{\Phi}_{i-\frac{1}{2}}, \tag{3.18a}$$

$$\mathbf{\Phi}_R = \overline{\mathbf{\Phi}}_{i+1} - 0.5\Delta\mathbf{\Phi}|_{i+1} = \overline{\mathbf{\Phi}}_{i+1} - 0.5\phi(r_R)\Delta\mathbf{\Phi}_{i+\frac{3}{2}}, \tag{3.18b}$$

where $\overline{\mathbf{\Phi}}$ means a cell-averaged value.

In the extremely varying region, $|\Delta\mathbf{\Phi}| \gg 1$, the following inequality is quite often observed without a limiter.

$$\overline{\mathbf{\Phi}}_i < \overline{\mathbf{\Phi}}_{i+1} < \mathbf{\Phi}_L \quad \text{or} \quad \mathbf{\Phi}_R < \overline{\mathbf{\Phi}}_i < \overline{\mathbf{\Phi}}_{i+1}. \tag{3.19}$$

Within the TVD condition, we can derive the following inequality from Eq. (3.19). The Superbee limiter is a good example of Eq. (3.20),

$$\overline{\mathbf{\Phi}}_i \leqslant \mathbf{\Phi}_R < \mathbf{\Phi}_L \leqslant \overline{\mathbf{\Phi}}_{i+1}. \tag{3.20}$$

In M-AUSMPW+, Eq. (3.20) is used as the definition of the rapidly varying region. The smooth region is determined accordingly.

Based on the criterion to distinguish the smooth region from the rapidly varying region, M-AUSMPW+ modifies the convective quantity only in the smooth region because a stability problem may occur in the rapidly varying region. If we choose the average value of $\mathbf{\Phi}_L$ and $\mathbf{\Phi}_R$ as a modified quantity, the accuracy can be greatly improved.

Fairly smooth region:

$$\mathbf{\Phi}_{L,i+\frac{1}{2}} = 0.5(\mathbf{\Phi}_L + \mathbf{\Phi}_R). \tag{3.21a}$$

Rapidly varying region:

$$\mathbf{\Phi}_{L,i+\frac{1}{2}} = \mathbf{\Phi}_L. \tag{3.21b}$$

Considering robust calculations, the modified convective quantity should satisfy the monotonic condition and upwind characteristic in a supersonic flow additionally.

For the monotonic condition, the modified quantity should be within the TVD condition as follows.

$$\min(\mathbf{\Phi}_{L,minmod}, \mathbf{\Phi}_{L,superbee}) \leqslant \mathbf{\Phi}_{L,\frac{1}{2}} \leqslant \max(\mathbf{\Phi}_{L,minmod}, \mathbf{\Phi}_{L,superbee}), \tag{3.22}$$

where $\mathbf{\Phi}_{minmod}$ and $\mathbf{\Phi}_{superbee}$ are values calculated by the minmod limiter and superbee limiter at a cell-interface, respectively.

In the viewpoint of the upwind characteristic, the form of $\mathbf{\Phi}_{\frac{1}{2}} = 0.5(\mathbf{\Phi}_L + \mathbf{\Phi}_R)$ is not correct for supersonic flow, although it is appropriate for a subsonic flow. This suggests that $\mathbf{\Phi}_{\frac{1}{2}}$ should be determined after a cell-interface state is identified, whether it belongs to the subsonic or the supersonic region.

Summarizing the mentioned requirements, the convective quantity at a cell-interface is finally formulated as follows.

$$\mathbf{\Phi}_{L,\frac{1}{2}} = \mathbf{\Phi}_L + \frac{\max[0,(\mathbf{\Phi}_R - \mathbf{\Phi}_L)(\mathbf{\Phi}_{L,superbee} - \mathbf{\Phi}_L)]}{(\mathbf{\Phi}_R - \mathbf{\Phi}_L) \mid \mathbf{\Phi}_{L,superbee} - \mathbf{\Phi}_L \mid} \min\left[a\frac{\mid \mathbf{\Phi}_R - \mathbf{\Phi}_L \mid}{2}, \mid \mathbf{\Phi}_{L,superbee} - \mathbf{\Phi}_L \mid\right], \tag{3.23a}$$

$$\mathbf{\Phi}_{R,\frac{1}{2}} = \mathbf{\Phi}_R + \frac{\max[0,(\mathbf{\Phi}_L - \mathbf{\Phi}_R)(\mathbf{\Phi}_{R,superbee} - \mathbf{\Phi}_R)]}{(\mathbf{\Phi}_L - \mathbf{\Phi}_R) \mid \mathbf{\Phi}_{R,superbee} - \mathbf{\Phi}_R \mid} \min\left[a\frac{\mid \mathbf{\Phi}_L - \mathbf{\Phi}_R \mid}{2}, \mid \mathbf{\Phi}_{R,superbee} - \mathbf{\Phi}_R \mid\right], \tag{3.23b}$$

where $a = 1 - \min(1,\max(|M_L|,|M_R|))^2$ and its derivative is continuous when the Mach number becomes zero. The details are provided in Ref. [22].

3.3. Development of wavenumber-extended finite volume schemes and coupling with M-AUSMPW+

In M-AUSMPW+, the physical state at a cell-interface is re-evaluated with the average value, $\mathbf{\Phi}_{L,R,\frac{1}{2}} = 0.5(\mathbf{\Phi}_L + \mathbf{\Phi}_R)$, in the smooth region. Therefore, the developed conservative wavenumber-extended optimization technique should be applied to the re-evaluated value $\mathbf{\Phi}_{L,R,\frac{1}{2}}$ for the minimization of the difference between the actual wavenumber and the effective wavenumber, which is defined as Eq. (3.13) in the present paper.

By comparing the effective wavenumbers of other optimized schemes with Eq. (3.13), we can see that the effective wavenumbers of the finite volume scheme coincide with those of the finite difference scheme, whose approximation is given by

$$\left(\frac{\partial f}{\partial \xi}\right) \approx \frac{1}{\Delta\xi}\sum_{j=-1}^{k-1} \mathrm{d}_{rj} f_{i-r+j}, \tag{3.24}$$

where coefficients are defined as $d_{rj} = C_{rj} - C_{r(j+1)}$ $(j = 0, \ldots, k-1)$, $d_{r(-1)} = -C_{r0}$, $d_{r(k-1)} = -C_{r(k-1)}$.

Thus, Eq. (3.24) has a similar form to the semi-discrete conservative finite difference scheme in Ref. [27] which is based on the conservative approximation of the derivative from point values. However, the derivation of Eq. (3.13) is not based on the approximation of the derivative but the approximation of the cell-interface values using cell averages, $\overline{\mathbf{\Phi}}$.

Suppose we use an interpolation which has a stencil size k and develop the pth order wavenumber-extended interpolation for all the candidate stencils,

$$\{\xi_{i-r}, \ldots, \xi_{i-r+k-1}\}, \quad r = 0, 1, \ldots, k-1 \tag{3.25}$$

in the discontinuous or the rapidly varying region where the convective quantity at a cell-interface is formulated as $\mathbf{\Phi}_{L,i+\frac{1}{2}} = \mathbf{\Phi}_L$.

For equally spaced grid points, $\mathbf{\Phi}$ is given by

$$\mathbf{\Phi}(\xi) = a_1\xi^{p-1} + a_2\xi^{p-2}\cdots + a_p. \tag{3.26}$$

And, the cell-averaged value is (see Fig. 2)

$$\frac{1}{\Delta\xi}\int_{(m-1)\Delta\xi}^{m\Delta\xi} \mathbf{\Phi}(\xi)\mathrm{d}\xi = \overline{\mathbf{\Phi}}_{i+m}, \quad m = -r, \ldots, 0, \ldots, k-r-1. \tag{3.27}$$

By use of the reconstruction procedure from the cell averages presented in Section 3.1, the interpolation in the smooth region where the convective quantity at a cell-interface is formulated as $\mathbf{\Phi}_{L,R,\frac{1}{2}} = 0.5(\mathbf{\Phi}_L + \mathbf{\Phi}_R)$ is represented by the following form:

$$\mathbf{\Phi}_{L,R,\frac{1}{2}} = 0.5(\mathbf{\Phi}_L + \mathbf{\Phi}_R) = \sum_{j=0}^{k-1}[c_{rj}\overline{\mathbf{\Phi}}_{i-r+j} + c_{r(k-1-j)}\overline{\mathbf{\Phi}}_{i-r+j+1}]. \tag{3.28}$$

Then, p linear equations for coefficients c_{rj} can be obtained in the following form:

$$\sum_{j=0}^{k-1} b_{lj}c_{rj} = z_l, \quad \text{for } l = 1, \ldots, p, \tag{3.29}$$

where b_{lj} and z_l are constants.

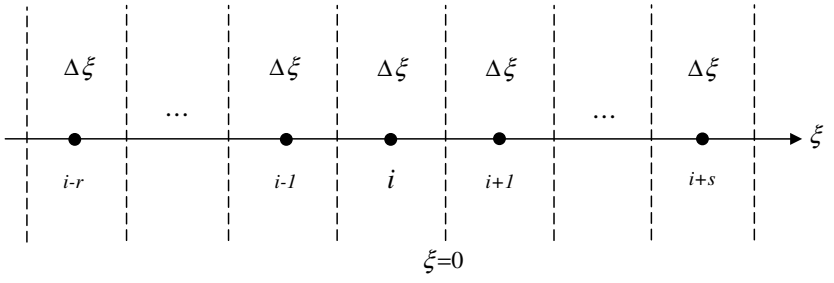

Fig. 2. Cell center point and cell-interfaces.

The rest of the $k-p$ equations are determined by minimizing E_r of Eq. (3.28). Then, E_r can be expressed as a function of the coefficients c_{rj},

$$E_r = E_r(c_{r0}, \ldots, c_{r(k-1)}). \tag{3.30}$$

If we assume that the first p coefficients c_{r0}, …, $c_{r(p-1)}$ are eliminated by Eq. (3.29), then Eq. (3.30) yields

$$E_r = E_r(c_{rp}, \ldots, c_{r(k-1)}). \tag{3.31}$$

As a result, the condition for E_r to be the minimum are

$$\frac{\partial E_r}{\partial c_{rj}} = 0, \quad \text{for } r = p, p+1, \ldots, k-1. \tag{3.32}$$

Therefore, Eq. (3.32) can give the optimized solution for the remaining $k-p$ coefficients.

Given a stencil size k, a variety of schemes can be constructed with different stencils and orders of accuracy. In the discontinuous or the rapidly varying region, however, upwind-biased schemes look more appropriate than centered schemes because upwind schemes can represent flow physics properly for the entire Mach number range (i.e., they transfer flow information correctly according to the local feature of wave physics) and capture discontinuity more accurately and robustly. In the present work, therefore, to make the most of the advantage of upwind schemes, the upwind-biased interpolation formulas which have an odd-number of stencil size k, are proposed for the discontinuous or the rapidly varying region. In the smooth region, these upwind-biased formulas change to the centered form formulas which are non-dissipative ($k_i = 0$) due to the symmetry of the coefficients throughout the re-evaluation step of M-AUSMPW+. As a result, the balancing coefficient in Eq. (3.15) yields automatically $\lambda = 1$. Therefore, the integrated error of the wavenumber-extended finite volume scheme is re-defined as

$$E_r = \int_0^{\eta} \{\lambda^*[k^*_{r,re} - \alpha\Delta\xi]^2 + (1-\lambda^*)[k^*_{i,pre}]^2\}\mathrm{d}(\alpha\Delta\xi), \tag{3.33}$$

where $k^*_{r,re}$ is the dispersion error of centered interpolation for the re-evaluation step and $k^*_{i,pre}$ is the dissipation error of upwind-biased interpolation for the discontinuous or the rapidly varying region. In addition, the new balancing coefficient λ^* is chosen to be 0.5 to minimize both the dispersion of the re-evaluated centered scheme in the smooth region and the dissipation of the non-evaluated upwind-biased scheme in the discontinuous or the rapidly varying region. As pointed out in Ref. [28], from the standpoint of wave propagation, it is more important to compare the group velocities of numerical schemes. The group velocity of a numerical scheme determined by $\mathrm{d}\bar{\alpha}/\mathrm{d}\alpha$ should be equal to 1 if the scheme is to reproduce the same group velocity of the speed of sound of an original PDE. In the present work, therefore, the optimization wavenumber range coefficient η in Eq. (3.33) is selected to maximize the resolved bandwidth ($|\frac{\mathrm{d}\bar{\alpha}}{\mathrm{d}\alpha} - 1.0| < 0.003$) of the re-evaluated centered interpolation in the re-evaluation step of M-AUSMPW+. The coefficients for some of the wavenumber-extended finite volume (WEFV) schemes with $k = 5$ (WEFV4), $k = 7$ (WEFV6) and $p = k-1$ are listed in Tables 1 and 2.

Fig. 3 shows the comparison of the relative dispersion errors of the re-evaluated WEFV schemes with $k = 5$, $k = 7$, $r = (k-1)/2$ and $p = k-1$ with those of the re-evaluated standard 3rd order (RS3), standard 5th order (RS5) and standard 7th order (RS7) interpolation in the re-evaluation step of M-AUSMPW+. This comparison demonstrates that the WEFV scheme matches the dispersion relation better than the standard high-order

Table 1
The coefficients for the 4th order wavenumber-extended finite volume (WEFV4) schemes with $k = 5$

	j	$r = 2$	$r = 3$	$r = 4$
c_{rj}	0	0.041951640579027	−0.05643372101490779	0.04775042143983386
	1	−0.251139895649441	0.309068217392964	−0.441001685759335
	2	0.835043176807494	−0.755268992756113	1.36983586197234
	3	0.415526771017226	1.30906821739296	−2.10766835242600
	4	−0.0413816927543065	0.193566278985092	2.13108375477317
η		0.355π	0.361π	0.367π

Table 2
The coefficients for the 6th order wavenumber-extended finite volume (WEFV6) schemes with $k = 7$

	j	$r = 3$	$r = 4$	$r = 5$	$r = 6$
c_{rj}	0	−0.010336730431374	−0.00201408799053892	−0.0088695550032267	0.08586573497425981
	1	0.078687049254910	−0.004582138723433148	0.0865506633526936	−0.681861076512225
	2	−0.288384289803943	0.08645534680858288	−0.349709991715067	2.32131935794723
	3	0.823401275294147	−0.343051573522555	0.794057766731201	−4.43398136615186
	4	0.461615710196057	0.919788680141916	−1.18304332504840	5.23798602461390
	5	−0.071312950745089	0.378751194609900	1.50321733001936	−3.06519440984556
	6	0.006329936235293	−0.03534742132387225	0.157797111663440	1.53586573497426
η		0.429π	0.431π	0.442π	0.451π

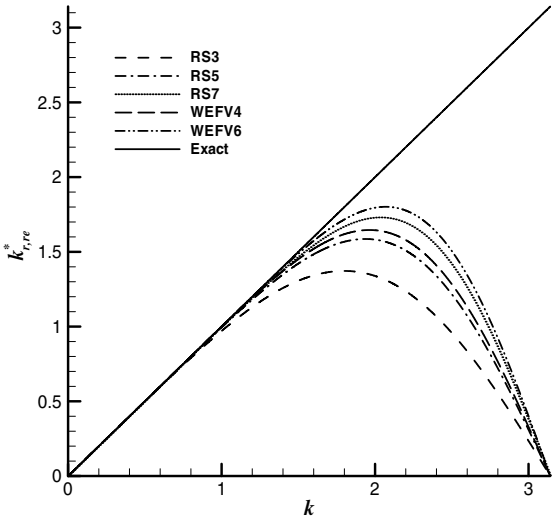

Fig. 3. The comparison of the relative dispersion errors of the re-evaluated WEFV schemes with $k = 5$, $k = 7$, $r = (k-1)/2$ and $p = k - 1$ with the re-evaluated standard 3rd order (RS3), standard 5th order (RS5) and standard 7th order (RS7) interpolation by the re-evaluation step of M-AUSMPW+.

interpolation with the same stencil size k and the left shift of stencil r. The low-dispersive characteristics of the WEFV scheme are represented more clearly throughout the comparison of the resolution, $\lambda_c/\Delta\xi$ which was defined by Tam [28]. Here, the critical wavenumber $\bar{\alpha}_c\Delta\xi$ is defined as the extent of deviation from the straight line $\bar{\alpha}\Delta\xi = \alpha\Delta\xi$ when the error is below some tolerance τ. The critical wavenumber and resolution for some of the WEFV schemes with $\tau = 0.01$ and $\tau = 0.001$ are listed in Tables 3 and 4, respectively. As shown, although the formal order of accuracy of the WEFV schemes is lower than that of the standard interpolation with same k and r, the WEFV scheme has the larger critical wavenumber and the lower resolution value.

Fig. 4 shows the $d\bar{\alpha}/d\alpha$ curves of the optimized schemes for the re-evaluation step as a function of $\alpha\Delta\xi$. As mentioned, when reducing the numerical dispersion error, the range of optimization, $0 \leqslant \alpha\Delta\xi \leqslant \eta$, is selected instead of the range of $0 \leqslant \alpha\Delta\xi \leqslant \pi/2$. And then, the optimization wavenumber range coefficient η is selected to maximize the resolved bandwidth. As a result, although the optimized scheme has a faster group velocity in some frequency ranges, the increase in group velocity is bound up to the resolved bandwidth. The resolved

Table 3
The critical wavenumber and resolution for wavenumber-extended finite volume schemes and the standard interpolations with $\tau = 0.01$

Scheme	$\bar{\alpha}_c\Delta\xi$	$\lambda_c/\Delta\xi$
RS3	0.798278693277166	7.89198064918489
RS5	1.08416362475384	5.81093098509963
RS7	1.29088042136005	4.88039007777533
WEFV4	1.25286715025161	5.02846610571184
WEFV6	1.47403527306433	4.27398184773632

Table 4
The critical wavenumber and resolution for wavenumber-extended finite volume schemes and the standard interpolations with $\tau = 0.001$

Scheme	$\bar{\alpha}_c \Delta\xi$	$\lambda_c/\Delta\xi$
RS3	0.498884913390059	12.6281629909186
RS5	0.767805244537345	8.20520574041686
RS7	0.977977793062503	6.44186406346894
WEFV4	0.837862760712398	7.51913116969584
WEFV6	1.05714592793297	5.95944214846324

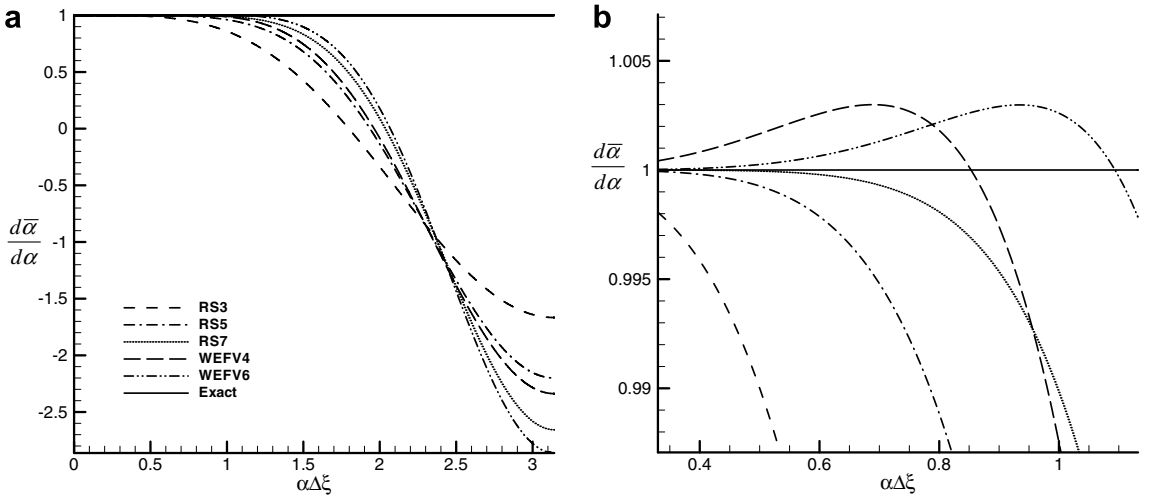

Fig. 4. (a) $d\bar{\alpha}/d\alpha$ versus $\alpha\Delta\xi$ for of the re-evaluated WEFV schemes with $k = 5$, $k = 7$, $r = (k-1)/2$ and $p = k - 1$ with the re-evaluated standard 3rd order (RS3), standard 5th order (RS5) and standard 7th order (RS7) interpolation by the re-evaluation step of M-AUSMPW+. (b) Zoomed View.

bandwidth of the WEFV4 becomes about 42.44% wider than that of the RS5, and the resolved bandwidth of the WEFV6 becomes about 34.89% wider than that of the RS7.

Fig. 5 shows the comparison of the relative dissipation errors of the optimized schemes for the discontinuous or the rapidly varying region with different approximation schemes. As shown in Figs. 4 and 5, the

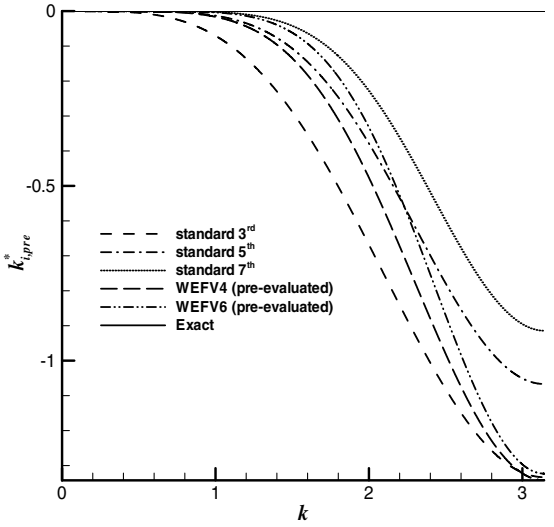

Fig. 5. The comparison of the relative dissipation errors of optimized schemes for the discontinuous of rapidly varying region with $k = 5$, $k = 7$, $r = (k-1)/2$ and $p = k - 1$ with the standard 3rd order, standard 5th order and standard 7th order interpolation.

optimized interpolation is somewhat more dissipative than the standard interpolation with the same k and r. Although the M-AUSMPW+ combined with wavenumber-extended optimization technique is somewhat more dissipative in the discontinuity or the rapidly varying region, it is more important that it has the less dispersive form in the smooth region because CAA focuses on the accurate prediction of aerodynamically generated sound as well as its long range propagation and far-field characteristics.

4. Method to treat the region of discontinuity

In order to control unwanted oscillations around a discontinuity, MLP is selected, which is developed by analyzing conventional TVD limiters with the multi-dimensional limiting function based on the flow information [21]. The major advantage of MLP is the removal of oscillations across a multi-dimensional discontinuity, and it is readily compatible with higher than the 3rd order spatial interpolation. Moreover, compared with other higher-order interpolation schemes such as ENO-type schemes, MLP shows a good convergence characteristic in a steady problem, and it is very simple to implement. However, MLP may provide excessive numerical dissipation in the continuous region because it was originally designed to control oscillations like TVD. That is, it is not suitable for time-accurate numerical solutions of aeroacoustic problems that contain linear waves of very small amplitudes in the far-field.

Therefore, in order to exclude this excessive dissipation of MLP from the region of continuity and provide low dissipative/more accurate results in the far-field, the distinguishing mechanism which is based on the Gibbs phenomenon is introduced. By using the newly introduced distinguishing mechanism, the application of MLP is restricted to only in the region of discontinuity where the Gibbs phenomenon is observed in computations.

4.1. Distinguishing mechanism between continuity and discontinuity

The partial Fourier sum,

$$\sum_{k=-N}^{N} \hat{f}_k e^{\pi i k x}, \tag{4.1}$$

based on the first $2N+1$ Fourier coefficients of a non-smooth function $f(x)$, converges slowly away from the discontinuity and features non-decaying oscillations [29–32]. This behavior of all global approximation of non-smooth functions is known as the classical Gibbs phenomenon. For example, it is observed that calculating values of such a function using a truncated series leads to results that oscillate near the discontinuity. As one includes more and more terms into the series, the oscillations persist but they move closer and closer to the discontinuity itself. Indeed, it is found that the series representation yields an overshoot at the jump, a value that is consistently larger than that of the actual function at the jump. No matter how many terms one adds to the series, this overshoot does not disappear. Thus, partial sums that approximate $f(x)$ do not approach $f(x)$ uniformly over an interval that contains a point where the function is discontinuous.

A central scheme, due to its nature, is not able to handle a discontinuity and generates numerical oscillations. Thus, if a central scheme is applied to a discontinuity, the Gibbs phenomenon, i.e. overshoot and undershoot, can be easily observed near edges of numerical discontinuity. Evidently, high-order central schemes have the Gibbs oscillation when applied to computations with discontinuity such as shock or contact surface although they are the most suitable for representing continuous solutions. In discontinuity, therefore, the interpolated value and the original distribution show a great discrepancy and, as a result, it is thought that the difference between interpolated plot and original distributions is good indicator for distinguishing discontinuity from continuity. In the developed scheme, the discontinuity is defined as the region where the Gibbs phenomenon is observed when a high-order central formulation is applied for the approximation, $\mathbf{\Phi}_{approx}$ to $\mathbf{\Phi}$ whose distribution is already known.

$$\mathbf{\Phi}_{approx,i} = \frac{-\mathbf{\Phi}_{i-2} + 4\mathbf{\Phi}_{i-1} + 4\mathbf{\Phi}_{i+1} - \mathbf{\Phi}_{i+2}}{6} = \mathbf{\Phi}_i + O(\Delta\xi^4). \tag{4.2}$$

In the present paper, the sensing term s_i is defined as the difference between the interpolated value of Eq. (4.2) and the original value $\mathbf{\Phi}_i$ at point i. Then, the criterion to distinguish the discontinuous region from the continuous region is proposed as follows:

In the continuous region:

$$s_i = |\ \mathbf{\Phi}_{approx,i} - \mathbf{\Phi}_i\ | \cong O(\Delta\xi^4), \tag{4.3a}$$

In the discontinuous region:

$$s_i = |\ \mathbf{\Phi}_{approx,i} - \mathbf{\Phi}_i\ | \geqslant O(\Delta\xi^2) \gg O(\Delta\xi^4). \tag{4.3b}$$

In the present work, the thresh-holding is chosen as $O(\Delta\ \xi^2)$.

Then, the left and right cell-interface values are obtained as follows.

In the continuous region:

$$\mathbf{\Phi}_L = \overline{\mathbf{\Phi}}_i + 0.5\beta_L \Delta\mathbf{\Phi}_{i-\frac{1}{2}}, \tag{4.4a}$$

$$\mathbf{\Phi}_R = \overline{\mathbf{\Phi}}_{i+1} - 0.5\beta_R \Delta\mathbf{\Phi}_{i+\frac{3}{2}}. \tag{4.4b}$$

In the discontinuous region:

$$\mathbf{\Phi}_L = \overline{\mathbf{\Phi}}_i + 0.5\phi(\beta_L)\Delta\mathbf{\Phi}_{i-\frac{1}{2}}, \tag{4.4c}$$

$$\mathbf{\Phi}_R = \overline{\mathbf{\Phi}}_{i+1} - 0.5\phi(\beta_R)\Delta\mathbf{\Phi}_{i+\frac{3}{2}}, \tag{4.4d}$$

where ϕ is MLP limiting function and $\beta_{L,R}$ is given in Section 4.3.

4.2. Multi-dimensional limiting process (MLP)

As known well, the one-dimensional TVD constraint can be written as follows.

$$0 \leqslant \phi(r) \leqslant \min(2r, 2). \tag{4.5}$$

Since the extension of Eq. (4.5) in the dimensional splitting manner is insufficient to prevent oscillations in multi-dimensional flows, Eq. (4.5) needs to be modified and/or extended with appropriate consideration of the multi-dimensional situation.

From Eq. (4.5), the property at a cell-interface satisfies the following distribution.

$$\overline{\mathbf{\Phi}}_{i-1} \leqslant \mathbf{\Phi}_{i-\frac{1}{2}} \leqslant \overline{\mathbf{\Phi}}_i, \quad \overline{\mathbf{\Phi}}_i \leqslant \mathbf{\Phi}_{i+\frac{1}{2}} \leqslant \overline{\mathbf{\Phi}}_{i+1}. \tag{4.6}$$

We can introduce the concept of Eq. (4.6) in one-dimensional situation and extend it to multi-dimensional situation as follows.

$$\overline{\mathbf{\Phi}}^{\min}_{neighbor} < \mathbf{\Phi} < \overline{\mathbf{\Phi}}^{\max}_{neighbor}. \tag{4.7}$$

In order to realize Eq. (4.7) in two-dimensions, the values at vertex points, $\mathbf{\Phi}_1$, $\mathbf{\Phi}_2$, $\mathbf{\Phi}_3$ and $\mathbf{\Phi}_4$ in Fig. 6, are required to satisfy the following conditions.

$$\min(\overline{\mathbf{\Phi}}_{i,j}, \overline{\mathbf{\Phi}}_{i+1,j}, \overline{\mathbf{\Phi}}_{i,j-1}, \overline{\mathbf{\Phi}}_{i+1,j-1}) < \mathbf{\Phi}_1 < \max(\overline{\mathbf{\Phi}}_{i,j}, \overline{\mathbf{\Phi}}_{i+1,j}, \overline{\mathbf{\Phi}}_{i,j-1}, \overline{\mathbf{\Phi}}_{i+1,j-1}), \tag{4.8a}$$

$$\min(\overline{\mathbf{\Phi}}_{i,j}, \overline{\mathbf{\Phi}}_{i+1,j}, \overline{\mathbf{\Phi}}_{i,j+1}, \overline{\mathbf{\Phi}}_{i+1,j+1}) < \mathbf{\Phi}_2 < \max(\overline{\mathbf{\Phi}}_{i,j}, \overline{\mathbf{\Phi}}_{i+1,j}, \overline{\mathbf{\Phi}}_{i,j+1}, \overline{\mathbf{\Phi}}_{i+1,j+1}), \tag{4.8b}$$

$$\min(\overline{\mathbf{\Phi}}_{i,j}, \overline{\mathbf{\Phi}}_{i-1,j}, \overline{\mathbf{\Phi}}_{i,j+1}, \overline{\mathbf{\Phi}}_{i-1,j+1}) < \mathbf{\Phi}_3 < \max(\overline{\mathbf{\Phi}}_{i,j}, \overline{\mathbf{\Phi}}_{i-1,j}, \overline{\mathbf{\Phi}}_{i,j+1}, \overline{\mathbf{\Phi}}_{i-1,j+1}), \tag{4.8c}$$

$$\min(\overline{\mathbf{\Phi}}_{i,j}, \overline{\mathbf{\Phi}}_{i-1,j}, \overline{\mathbf{\Phi}}_{i,j-1}, \overline{\mathbf{\Phi}}_{i-1,j-1}) < \mathbf{\Phi}_4 < \max(\overline{\mathbf{\Phi}}_{i,j}, \overline{\mathbf{\Phi}}_{i-1,j}, \overline{\mathbf{\Phi}}_{i,j-1}, \overline{\mathbf{\Phi}}_{i-1,j-1}). \tag{4.8d}$$

Consequently, the one-dimensional limiting condition and the multi-dimensional limiting function are compared as follows.

One-dimensional limiting condition:

$$\max(0, \min(2r, 2)). \tag{4.9a}$$

Multi-dimensional limiting function:

$$\max(0, \min(\alpha r, \alpha)). \tag{4.9b}$$

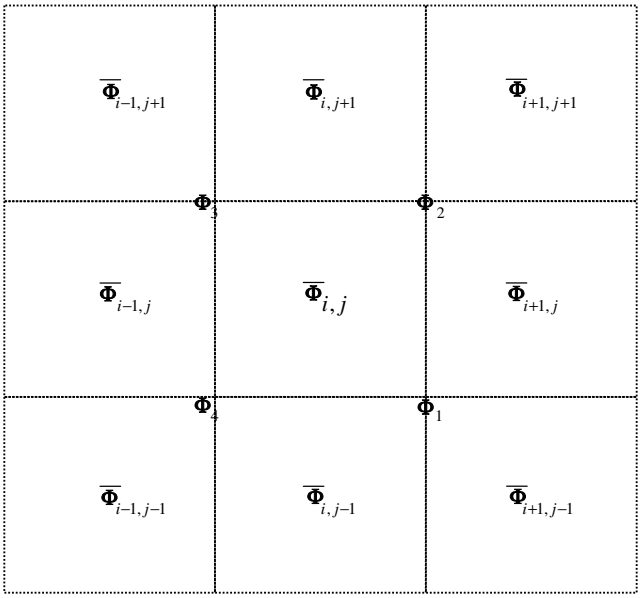

Fig. 6. Distributions of cell averaged values and cell vertex values.

Eq. (4.9b) is almost similar to the traditional TVD condition, except for the variable α by which MLP is able to control oscillations near discontinuity. Through the use of the variable α, MLP can consider the information on the property distribution in multi-dimensions and generate the numerical dissipation appropriate to the flow physics (see Fig. 7).

4.3. Combination of distinguishing mechanism, wavenumber-extended finite volume schemes and MLP

Similar to the TVD MUSCL approach, left and right cell-interface values are obtained as follows with the multi-dimensional limiting function of Eq. (4.9b)

In the continuous region ($s_i = |\mathbf{\Phi}_{approx,\ i} - \mathbf{\Phi}_i| < O(\Delta\xi^2)$):

$$\mathbf{\Phi}_L = \overline{\mathbf{\Phi}}_i + 0.5\beta_L \Delta\mathbf{\Phi}_{i-\frac{1}{2}}, \tag{4.10a}$$

$$\mathbf{\Phi}_R = \overline{\mathbf{\Phi}}_{i+1} - 0.5\beta_R \Delta\mathbf{\Phi}_{i+\frac{3}{2}}. \tag{4.10b}$$

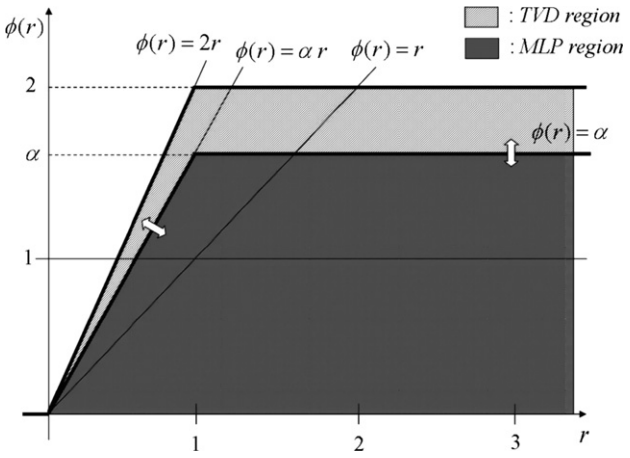

Fig. 7. Comparison of TVD and MLP regions.

In the discontinuous region ($s_i = |\mathbf{\Phi}_{approx,\ i} - \mathbf{\Phi}_i| \geqslant O(\Delta\xi^2)$):

$$\mathbf{\Phi}_L = \overline{\mathbf{\Phi}}_i + 0.5\phi(r_{L,i}, \alpha_L, \beta_L)\Delta\mathbf{\Phi}_{i-\frac{1}{2}} = \overline{\mathbf{\Phi}}_i + 0.5\max(0, \min(\alpha_L r_{L,i}, \alpha_L, \beta_L))\Delta\mathbf{\Phi}_{i-\frac{1}{2}}, \tag{4.10c}$$

$$\mathbf{\Phi}_R = \overline{\mathbf{\Phi}}_{i+1} - 0.5\phi(r_{R,i+1}, \alpha_R, \beta_R)\Delta\mathbf{\Phi}_{i+\frac{3}{2}} = \overline{\mathbf{\Phi}}_{i+1} - 0.5\max(0, \min(\alpha_R r_{R,i+1}, \alpha_R, \beta_R))\Delta\mathbf{\Phi}_{i+\frac{3}{2}}, \tag{4.10d}$$

where values of $\alpha_{L,R}$ and $\beta_{L,R}$ in Eq. (4.10) are summarized as follows.

Along the ξ-direction,

$$\alpha_L = g\left[\frac{2\max(1, r_{L,i})\left(1 + \max\left(0, \frac{\tan\theta_{i+1}}{r_{R,i+1}}\right)\right)}{1 + \tan\theta_i}\right], \quad \alpha_R = g\left[\frac{2\max(1, r_{R,i+1})\left(1 + \max\left(0, \frac{\tan\theta_i}{r_{L,i}}\right)\right)}{1 + \tan\theta_{i+1}}\right], \tag{4.11a}$$

where $r_{L,i} = \frac{\Delta\mathbf{\Phi}_{i+\frac{1}{2},j}}{\Delta\mathbf{\Phi}_{i-\frac{1}{2},j}}$, $r_{R,i+1} = \frac{\Delta\mathbf{\Phi}_{i+\frac{1}{2},j}}{\Delta\mathbf{\Phi}_{i+\frac{3}{2},j}}$ and $g(x) = \max(1,\min(2,x))$.

Along the η-direction,

$$\alpha_L = g\left[\frac{2\max(1, r_{L,j})\left(1 + \max\left(0, \frac{\tan\theta_{j+1}}{r_{R,j+1}}\right)\right)}{1 + \tan\theta_j}\right], \quad \alpha_R = g\left[\frac{2\max(1, r_{R,j+1})\left(1 + \max\left(0, \frac{\tan\theta_j}{r_{L,j}}\right)\right)}{1 + \tan\theta_{j+1}}\right], \tag{4.11b}$$

where $r_{L,j} = \frac{\Delta\mathbf{\Phi}_{i,j+\frac{1}{2}}}{\Delta\mathbf{\Phi}_{i,j-\frac{1}{2}}}$, $r_{R,j+1} = \frac{\Delta\mathbf{\Phi}_{i,j+\frac{1}{2}}}{\Delta\mathbf{\Phi}_{i,j+\frac{3}{2}}}$ and

$$\tan\theta_i = \left|\frac{(\overline{\mathbf{\Phi}}_{i,j+1} - \overline{\mathbf{\Phi}}_{i,j-1})}{(\overline{\mathbf{\Phi}}_{i+1,j} - \overline{\mathbf{\Phi}}_{i-1,j})}\right|, \quad \tan\theta_j = \left|\frac{(\overline{\mathbf{\Phi}}_{i+1,j} - \overline{\mathbf{\Phi}}_{i-1,j})}{(\overline{\mathbf{\Phi}}_{i,j+1} - \overline{\mathbf{\Phi}}_{i,j-1})}\right|.$$

Combining Eqs. (4.10) and (4.11) with β, we finally obtain MLP-5, MLP-7, MLP-O4 and MLP-O6 with $k = 5$or $k = 7$ and $r = (k-1)/2$ in Eq. (3.28).

*MLP with standard 5*th *order interpolation (MLP-5):*

$$\beta_L = \frac{-2/r_{L,i-1} + 11 + 24r_{L,i} - 3r_{L,i}r_{L,i+1}}{30}, \tag{4.12a}$$

$$\beta_R = \frac{-2/r_{R,i+2} + 11 + 24r_{R,i+1} - 3r_{R,i+1}r_{R,i}}{30}, \tag{4.12b}$$

*MLP with standard 7*th *order interpolation (MLP-7):*

$$\beta_L = \frac{6/r_{L,i-2}r_{L,i-1} - 44/r_{L,i-1} + 158 + 360r_{L,i} - 68r_{L,i}r_{L,i+1} + 8r_{L,i}r_{L,i+1}r_{L,i+2}}{420}, \tag{4.12c}$$

$$\beta_R = \frac{6/r_{R,i+3}r_{R,i+2} - 44/r_{R,i+2} + 158 + 360r_{R,i+1} - 68r_{R,i+1}r_{R,i} + 8r_{R,i+1}r_{R,i}r_{R,i-1}}{420}, \tag{4.12d}$$

*MLP with wavenumber-extended 4*th *order interpolation (MLP-O4):*

$$\begin{aligned}\beta_L = {} & -2c_{20}/r_{L,i-1} - 2(c_{20} + c_{21}) \\ & + 2(1 - c_{20} - c_{21} - c_{22})r_{L,i} + 2(1 - c_{20} - c_{21} - c_{22} - c_{23})r_{L,i}r_{L,i+1},\end{aligned} \tag{4.12e}$$

$$\begin{aligned}\beta_R = {} & -2c_{20}/r_{R,i+2} - 2(c_{20} + c_{21}) \\ & + 2(1 - c_{20} - c_{21} - c_{22})r_{R,i+1} + 2(1 - c_{20} - c_{21} - c_{22} - c_{23})r_{R,i+1}r_{R,i},\end{aligned} \tag{4.12f}$$

*MLP with wavenumber-extended 6*th *order interpolation (MLP-O6):*

$$\begin{aligned}\beta_L = {} & -2c_{30}/r_{L,i-2}r_{L,i-1} - 2(c_{30} + c_{31})/r_{L,i-1} - 2(c_{30} + c_{31} + c_{32}) + 2(1 - c_{30} - c_{31} - c_{32} - c_{33})r_{L,i} \\ & + 2(1 - c_{30} - c_{31} - c_{32} - c_{33} - c_{34})r_{L,i}r_{L,i+1} + 2(1 - c_{30} - c_{31} - c_{32} - c_{33} - c_{34})r_{L,i}r_{L,i+1}r_{L,i+2},\end{aligned} \tag{4.12g}$$

$$\begin{aligned}\beta_R = {} & -2c_{30}/r_{R,i+3}r_{R,i+2} - 2(c_{30} + c_{31})/r_{R,i+2} - 2(c_{30} + c_{31} + c_{32}) + 2(1 - c_{30} - c_{31} - c_{32} - c_{33})r_{R,i+1} \\ & + 2(1 - c_{30} - c_{31} - c_{32} - c_{33} - c_{34})r_{R,i+1}r_{R,i} + 2(1 - c_{30} - c_{31} - c_{32} - c_{33} - c_{34})r_{R,i+1}r_{R,i}r_{R,i-1},\end{aligned} \tag{4.12h}$$

where the coefficients c_{rj} are defined in Table 1 and 2.

5. Numerical results

In order to investigate the actual performances of the wavenumber-extended finite volume schemes, several test cases were carried out. They included spherical wave propagation, nonlinear wave propagation, shock tube problem and vortex preservation test problems. In a linear problem, i.e., a spherical wave propagation problem, the computed results obtained from the M-AUSMPW+ combined with a conservative wavenumber-extended optimized interpolation were compared with those obtained from AUSMPW+ combined with the standard 5th order interpolation. In nonlinear problems, the computed results obtained by M-AUSMPW+ combined with MLP-OS4 (MLP-O4 with the distinguishing mechanism) were compared with those obtained by the standard MLP-5 or MLP-5S (MLP-5 with the distinguishing mechanism). The 4-stage Runge–Kutta time integration was used for 1-D problems and the third order TVD Runge–Kutta time integration [33] was used for 2-D simulations. For boundary conditions, free stream values were specified as the inflow conditions, and extrapolation from inner computational domain was used for outflow conditions. At the wall, no-slip condition was specified for velocity, and adiabatic condition is used for temperature.

In addition to the calculations described above, the developed numerical method was applied to the more realistic shock–vortex interaction and muzzle blast flow problems. The shock–vortex interaction problem was performed at the same condition of $M_s = 1.29$ and $M_v = 0.39$ as in the experiment of Dosanjh and Weeks [34]. The computed results obtained by M-AUSMPW+ with MLP-OS4 were compared with those obtained by the inviscid Euler simulation by Ellzey et al. [35] and the Navier–Stokes simulation by O. Inoue and Y. Hattori [36]. For the muzzle blast flow problem, the simplified shooting noise generation and propagation mechanism were calculated at the projectile velocity, $M_p = 1.25$.

5.1. Spherical wave propagation

As mentioned in Section 3.3, the developed wavenumber-extended scheme is basically based on the finite volume approach and the conservative requirement, i.e., the approximation of cell-interface value using cell averages is used instead of the approximation of the derivative from the point values. As a result, the dispersive characteristic of the developed wavenumber-extended scheme may differ from that of a well-known standard optimized finite difference scheme such as DRP or compact scheme. In addition, the quantitative comparison between cell-averaged values of the finite volume scheme with M-AUSMPW+ and the point values of the finite difference scheme do not seem to be easy especially in Euler Equations. Therefore, a classical aeroacoustic problem, the spherical wave propagation [37], is calculated to investigate the dispersive characteristics of the developed method.

The model equation of spherical wave propagation has the form,

$$\frac{\partial u}{\partial t} + \frac{u}{r} + \frac{\partial u}{\partial r} = 0, \quad r > 5, \quad t > 0. \tag{5.1}$$

In this problem, the initial condition is null, i.e., $u(x,t=0) = 0$ and the boundary condition at $r = 5$ is,

$$u = 5\sin(\omega t), \tag{5.2}$$

where, $\omega = \pi/3$ is chosen.

The uniform-spacing grid with $\Delta r = 1$ is used, and the 4-stage Runge–Kutta scheme is used for time integration. The time step size is determined as $\Delta t = 0.001$, so the influence of numerical errors can be neglected in the time integration stage.

In Fig. 8a, b and c, the computed results of wave distributions at $t = 400$ are emphasized in $40 \leqslant r \leqslant 75$, $220 \leqslant r \leqslant 250$ and $380 \leqslant r \leqslant 420$, respectively. In Fig. 8a, the numerical methods are compared with each other in terms of the numerical dispersion and dissipation. M-AUSMPW+ combined with the standard 5th order interpolation and M-AUSMPW+ with WEFV4 show good agreement with the exact solution. On the other hand, AUSMPW+ with the standard 5th order interpolation and AUSMPW+ with WEFV4 show a large discrepancy from the exact solution because AUSMPW+ always maintains the upwind flux form, i.e., excessive numerical dissipation occurs.

In Fig. 8b and c, the dispersion error of M-AUSMPW+ with the standard 5th order interpolation increases steadily as the wave progresses further. In addition, both AUSMPW+ with the standard 5th order interpolation and AUSMPW+ with WEFV4 are extremely dissipated by the upwind characteristics. As expected, M-AUSMPW+ with WEFV4 shows low-dissipation and low-dispersion characteristics compared to the 4th order DRP scheme.

Fig. 9 shows the L_2 norms of error of the computed results. M-AUSMPW+ with WEFV4 provided a more accurate result than the 4th order DRP scheme. Compared with the DRP scheme, which is conventionally used in CAA, M-AUSMPW+ combined with wavenumber-extended finite volume schemes controlled dispersion characteristics more effectively. As the wave propagated, in spite of the upwind characteristic of the spatial discretization scheme, AUSMPW+ with WEFV4 was less dissipative than M-AUSMPW+ with the standard 5th order interpolation because of the reduction of the phase error in WEFV4.

Based on the previous test problem, it was confirmed again that M-AUSMPW+ combined with WEFV4 gave low-dissipation and low-dispersion characteristics compared to the 4th order DRP scheme while it

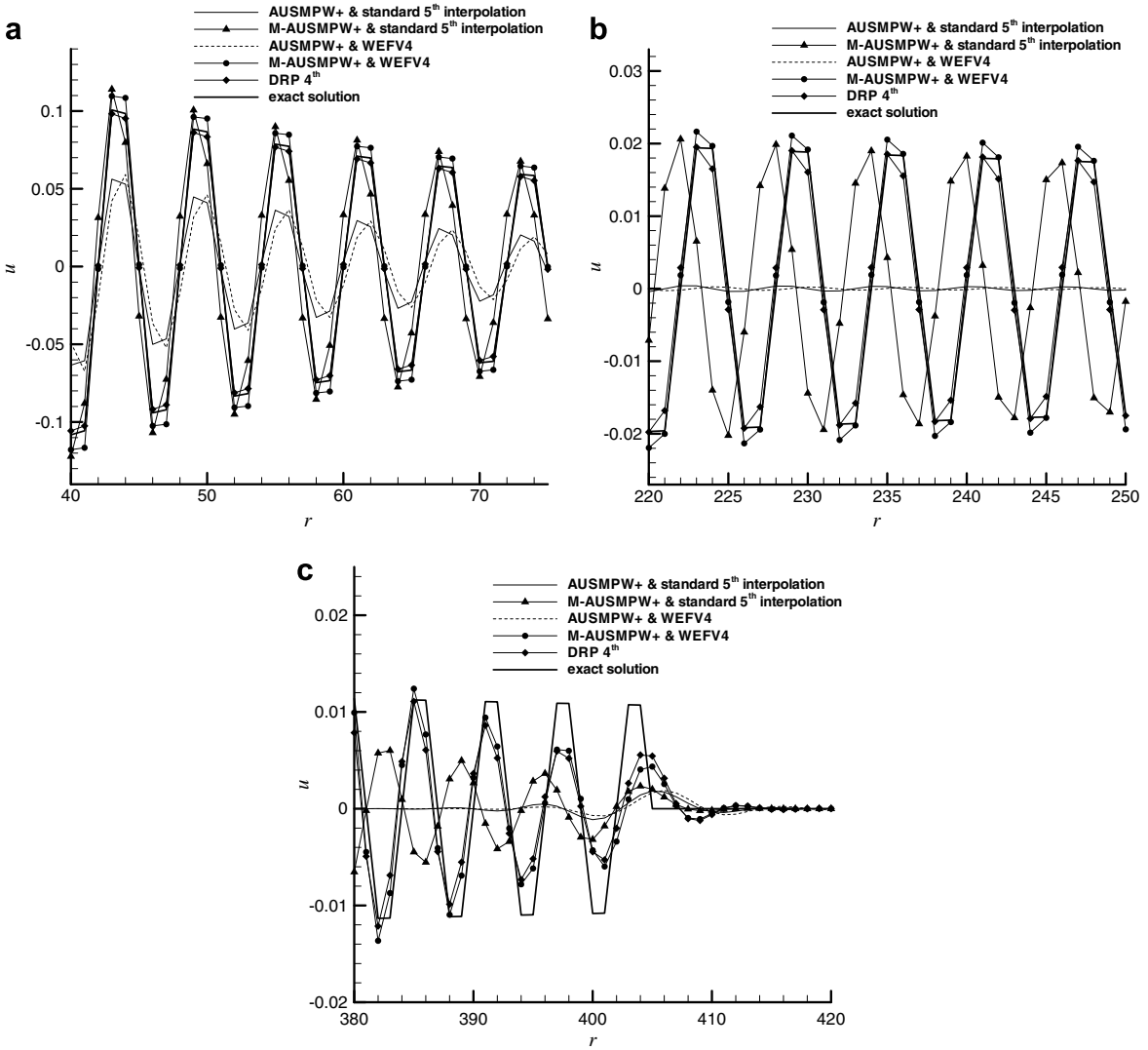

Fig. 8. The comparison of the M-AUSMPW+ combined with WEFV4 and standard 5th order interpolation, AUSMPW+ combined with WEFV4 and standard 5th order interpolation, and DRP for the spatial wave distribution at $t = 400$. (a) $40 \leqslant r \leqslant 75$ (b) $220 \leqslant r \leqslant 250$ (c) $380 \leqslant r \leqslant 420$.

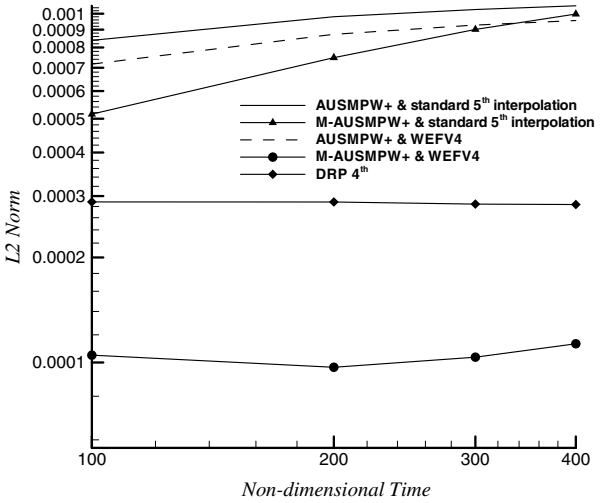

Fig. 9. The comparison of the M-AUSMPW+ combined with WEFV4 and standard 5th order interpolation, AUSMPW+ combined with WEFV4 and standard 5th order interpolation, and DRP for the L_2 Norm of error.

maintained the inherent advantages of finite volume schemes, i.e., the conservation and the applicability to non-uniform mesh.

5.2. Nonlinear wave propagation

The one-dimensional Euler equations are to be solved. The initial wave is the implied simple Gaussian wave which has the form [23],

$$u(x,t=0) = 0.5\exp\left(-\ln 2\cdot\left(\frac{x}{5}\right)^2\right), \tag{5.3a}$$

$$p(x,t=0) = \frac{1}{\gamma}\left(1+\frac{\gamma-1}{2}u(x,t=0)\right)^{\frac{2\gamma}{\gamma-1}}, \tag{5.3b}$$

$$\rho(x,t=0) = \left(1+\frac{\gamma-1}{2}u(x,t=0)\right)^{\frac{2}{\gamma-1}}. \tag{5.3c}$$

An approximate solution for nonlinear wave propagation can be obtained from simple assumptions: the flow is isentropic and the Riemann invariant, $\frac{2a}{\gamma-1}-u=\frac{2}{\gamma-1}$, is valid everywhere. Thus, the Euler equation reduces to the nonlinear simple wave equation [37],

$$\frac{\partial u}{\partial t}+\left(1+\frac{\gamma+1}{2}u\right)\frac{\partial u}{\partial x}=0. \tag{5.4}$$

This quasi-linear wave equation can be solved by the method of characteristics analytically. As a wave propagates, the initial wave evolves into a shock at the front of the pulse.

The whole computation domain is given in the range $(-50, 350)$ with the uniform grid spacing, $\Delta x = 1$. The 4-stage Runge–Kutta scheme is used for time integration and the time step size, Δt, is 0.001.

In order to investigate the effect of the conservative wavenumber-extended optimization and the distinguishing mechanism on shock capturing capability and monotonic characteristics, numerical tests were performed for 4 cases: M-AUSMPW+ with MLP-5, MLP-O4, MLP-5S and MLP-OS4.

Figs. 10 and 11 show the density perturbation distributions at $t = 200$ and $t = 100$, respectively. The velocity distribution at $t = 200$ is shown in Fig. 12. Numerical solutions were compared with the analytical approximate solution obtained by Whitham's kinematic wave method [38]. There was a good overall agreement with the analytical approximate solution, which was obtained by the equal area rule. Although there was a discrep-

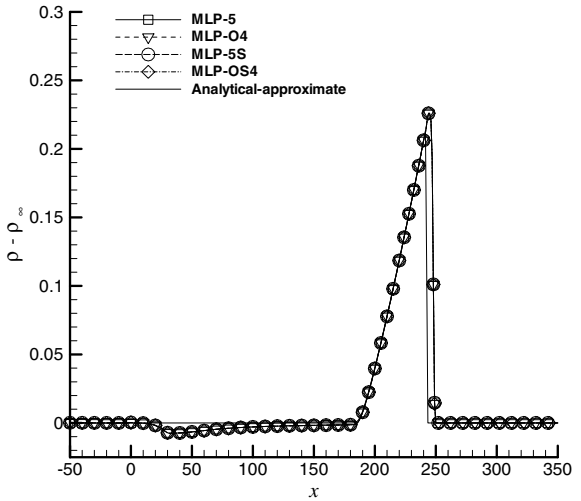

Fig. 10. The comparison of density distribution of M-AUSMPW+ combined with MLP-OS4, MLP-O4, MLP-5S and MLP-5 for the propagation of a nonlinear wave at $t = 200$.

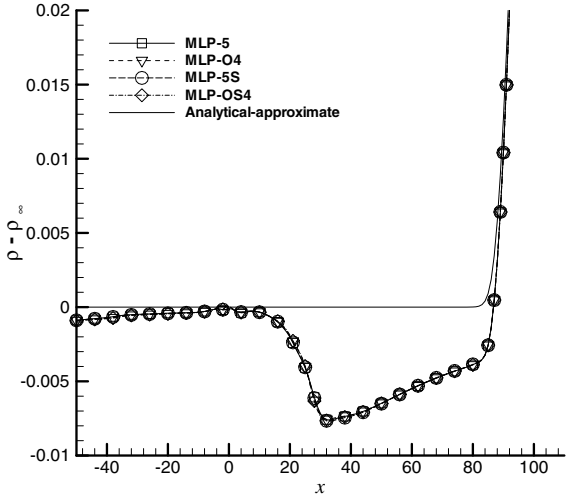

Fig. 11. The comparison of density distribution of M-AUSMPW+ combined with MLP-OS4, MLP-O4, MLP-5S and MLP-5 for the propagation of a nonlinear wave at $t = 100$.

ancy between calculated results and the analytic solution, those results were reasonable because the analytic solution may not have captured the true thickness of the shock due to the nonlinear characteristics of the flow around the shock. In addition, as shown in Figs. 10 and 11, all the applied schemes provided monotonic profiles and nearly the same results. Based on this test case, it is expected that the use of the wavenumber-extended optimized process and the selective application of MLP by the distinguishing mechanism will not compromise the monotonic shock capturing capability of the original MLP.

5.3. Shock tube problem

This problem is performed to investigate not only the shock-capturing characteristic but also the ability to distinguish an expansion wave from a compression shock wave.

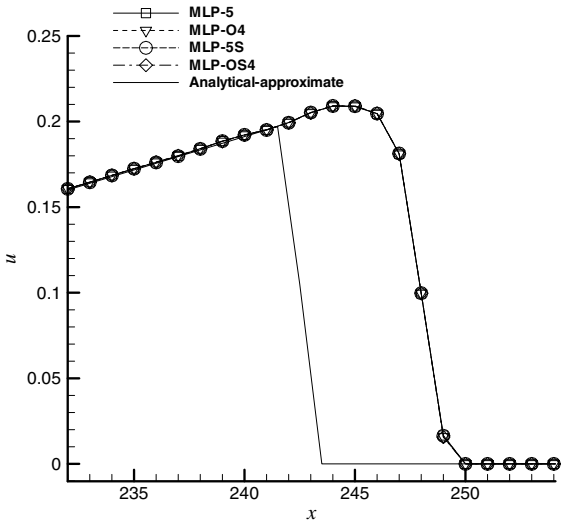

Fig. 12. The comparison of velocity distribution of M-AUSMPW+ combined with MLP-OS4, MLP-O4, MLP-5S and MLP-5 for the propagation of a nonlinear wave at $t = 200$.

The initial condition of the shock tube problem is given by

$$u = 0, \tag{5.5a}$$

$$p = \begin{cases} 4.4, & x < -2 \\ 2.7 + 1.7\cos[(x+2)\pi/4], & -2 \leqslant x \leqslant 2, , \\ 1, & x > 2 \end{cases} \tag{5.5b}$$

$$\rho = (\gamma p)^{1/\gamma}, \quad \gamma = 1.4. \tag{5.5c}$$

The whole computation domain is given in the range of $(-100, 100)$. Figs. 13 and 14 show the spatial distributions of density ρ at $t = 40$ and $t = 60$, respectively. Fig. 15 shows the spatial distribution of velocity u at time $t = 60$. As expected, the numerical simulation of a nonlinear acoustic pulse problem showed no oscillation near the shock in Fig. 13 and no undershoot/overshoot phenomenon in the density distribution in Fig. 14.

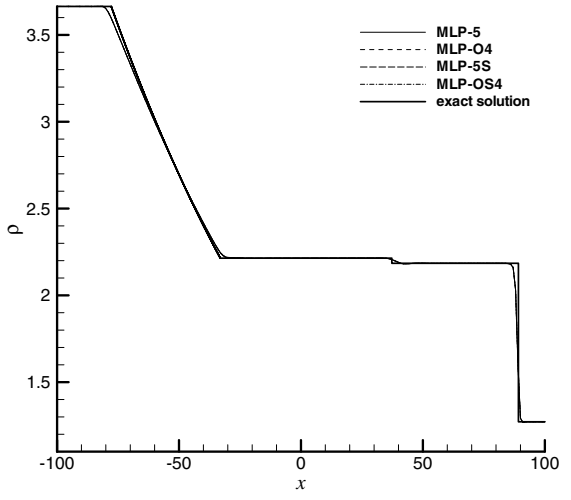

Fig. 13. The comparison of density distribution of M-AUSMPW+ combined with MLP-OS4, MLP-O4, MLP-5S and MLP-5 for the shock tube problem at $t = 60$.

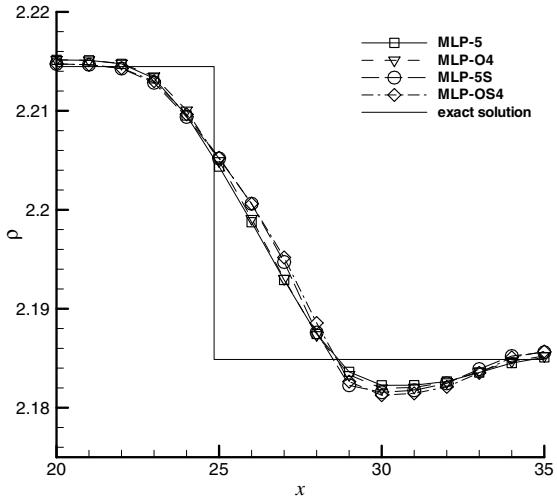

Fig. 14. The comparison of density distribution of M-AUSMPW+ combined with MLP-OS4, MLP-O4, MLP-5S and MLP-5 for the shock tube problem at $t = 40$.

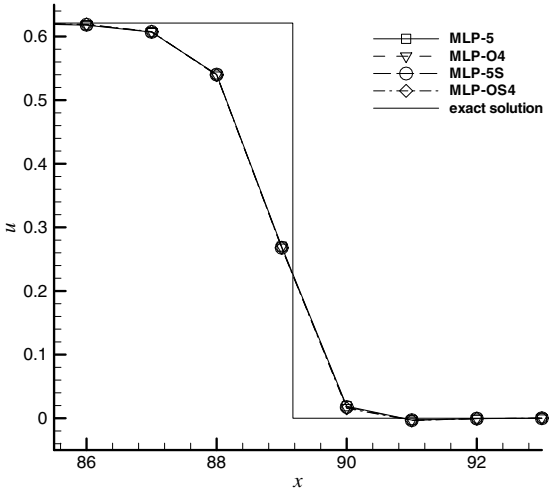

Fig. 15. The comparison of velocity distribution of M-AUSMPW+ combined with MLP-OS4, MLP-O4, MLP-5S and MLP-5 for the shock tube problem at $t = 60$.

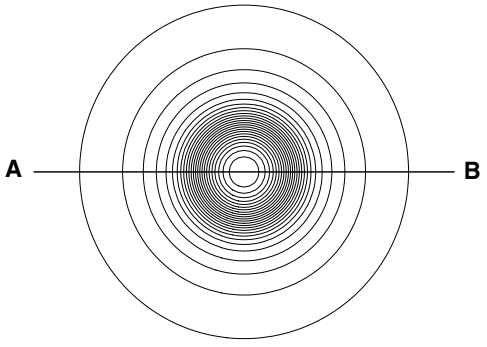

Fig. 16. Density contours of vortex flow.

In addition, Fig. 15 shows a sharp shock formation. Also, M-AUSMPW+ combined with the wavenumber-extended optimization did not yield entropy decreasing phenomena, such an expansion shock, because the numerical speed of sound defined in M-AUSMPW+ is able to distinguish an expansion shock wave from a compression shock wave.

5.4. Stationary vortex flow

To improve the accuracy of a vortex flow is one of the main objectives in the present work since it is a good example of multi-dimensional continuous flows. Fig. 16 shows the typical computed result. It is the Thomson–Rankine vortex model which is composed of the free vortex outside the core and the forced vortex inside.

Free vortex (outside the core):

$$V_\theta \cdot r = const. \text{ and } \frac{1}{\rho}\frac{\partial p}{\partial r} = \frac{V_\theta^2}{r}. \tag{5.6a}$$

Forced vortex (inside the core):

$$V_\theta = \omega \cdot r \text{ and } \frac{dp}{dr} = \rho\frac{V_\theta^2}{r}. \tag{5.6b}$$

Angular velocity ω is 2 and core radius is 0.2. Maximum velocity is $0.36c_\infty$ [21]. Computational domain is given in the range of $(-1, 1)$ with 50 by 50 grid points with the equal grid spacing. For the grid convergence test, 20 by 20, 40 by 40, 80 by 80, 160 by 160 and 200 by 200 grid points were used. M-AUSMPW+ was used for the spatial discretization. MLP-OS4 was compared with MLP-O4, MLP-5 and MLP-5S. For time integration, the 3rd order TVD Runge–Kutta method was used. The time step size, Δt is 0.01, and the boundary values were fixed as the initial values. The pressure distributions were plotted at the non-dimensional time of 30. Since viscous diffusion was not introduced, entropy was constant and a vortex flow should be maintained, so long as a centrifugal force was balanced with the pressure gradient toward the vortex core. Thus, the ideal solution is the initial distribution itself in the Euler equations.

Fig. 17 shows the results using MLP-5, MLP-5S, MLP-O4 and MLP-OS4 with 50 by 50 grid points. We can see the difference according to the interpolation schemes. Firstly, it is easy to find that MLPs without the distinguishing mechanism (MLP-5 and MLP-O4) is more dissipative than MLPs with the distinguishing mechanism (MLP-5S and MLP-OS4). And, the use of the distinguishing mechanism seems to be essential in time-accurate numerical simulations of aeroacoustic problems that contain multi-dimensional continuous flow fields. Secondly, the difference between MLP-5 and MLP-O4 or between MLP-5S and MLP-OS4 is negligible.

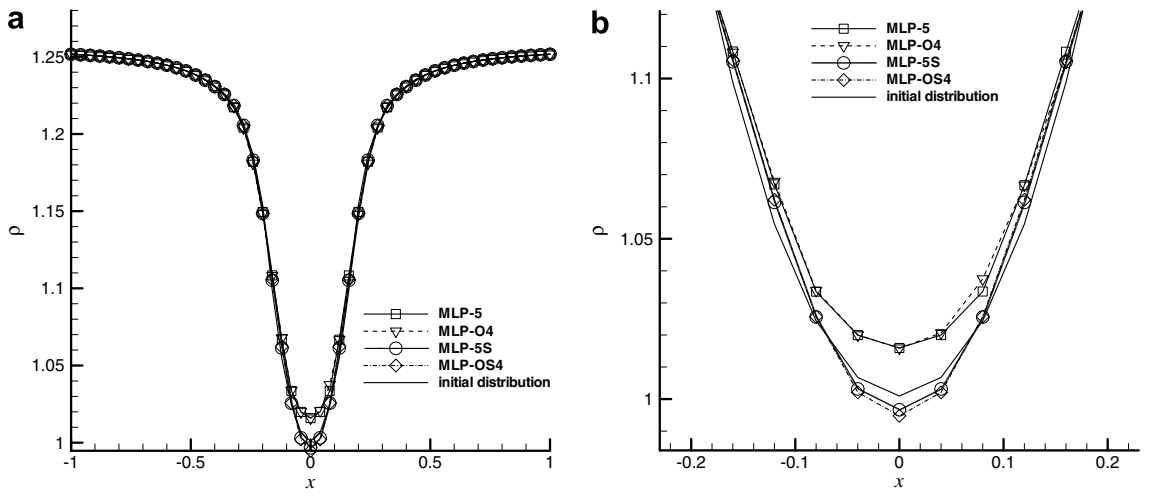

Fig. 17. (a) Comparison of density distributions along the line AB (50 by 50). (b) Zoomed view.

As mentioned in Section 3, the wavenumber-extended optimization procedure reduces the kth order spatial interpolation to pth order formal accuracy, where $p \leqslant k-1$. As a result, the application of the wavenumber-optimization technique leads to minutely larger dissipation than the standard interpolation with same k and r. However, the difference is negligible as shown in Fig. 17.

Figs. 18 and 19 show the results of the grid convergence test. Fig. 18 shows the density distribution using MLP-OS4 with 20 by 20, 80 by 80 and 200 by 200 grid points. Fig. 19 shows the L_2 norm of the density error of various schemes.

In M-AUSMPW+, the formal order of accuracy is increased by one order of magnitude with the averaged value of $\mathbf{\Phi}_{L,\frac{1}{2}} = \mathbf{\Phi}_{R,\frac{1}{2}} = 0.5(\mathbf{\Phi}_L + \mathbf{\Phi}_R)$. Theoretically, M-AUSMPW+ can provide more accurate solutions than the order of magnitude of an interpolation scheme. However, due to a slope limiting effect by the multi-dimensional limiting function, M-AUSMPW+ combined with MLP-5 becomes slightly more diffusive than the standard fifth order interpolation result. It is located between third and fifth order accuracy. On the other hand, the distinguishing mechanism excludes the excessive dissipation of the limiting process in the region of

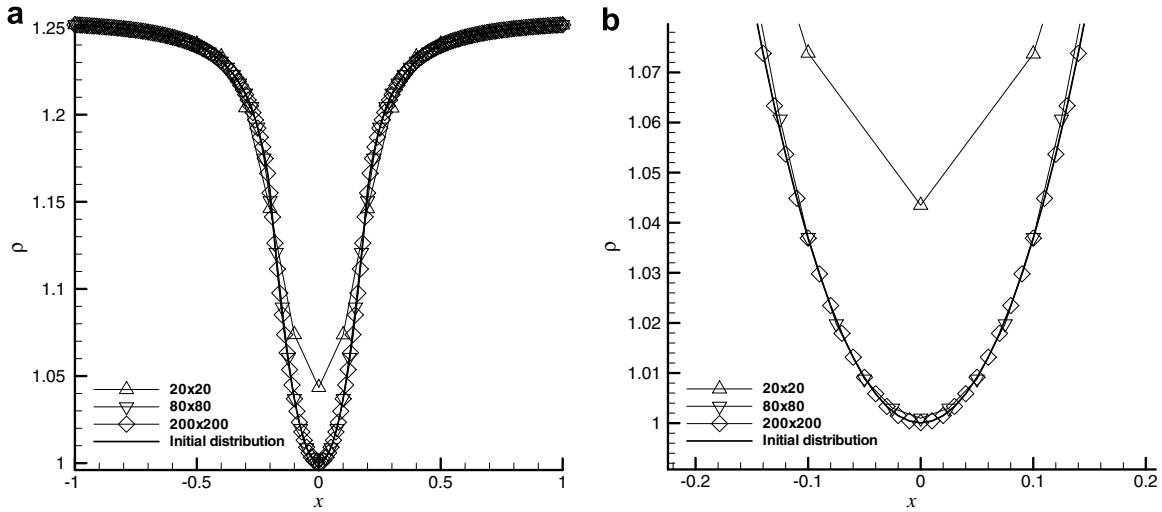

Fig. 18. (a) Density distributions of M-AUSMPW+ combined with MLP-OS4 along the line AB. (b) Zoomed view.

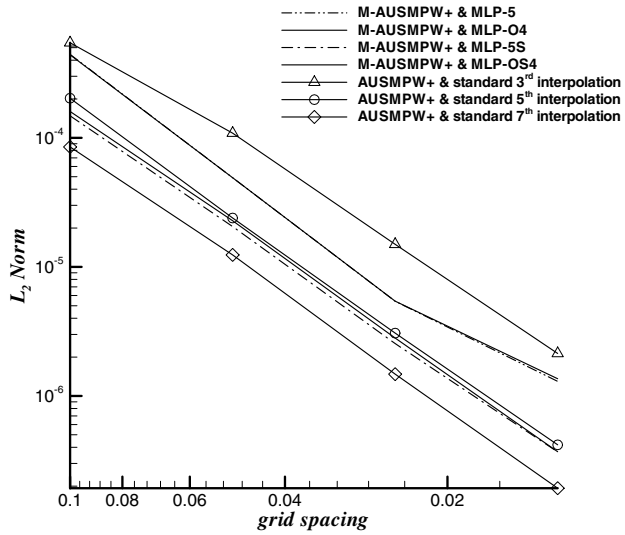

Fig. 19. Grid convergence of M-AUSMPW+ combined with MLP-OS4, MLP-O4, MLP-5S and MLP-5.

continuity and thus, improves the solution. Finally, the results by MLP-5S are located between fifth and seventh order spatial accuracy. In addition, even though the wavenumber-extended optimization reduces the formal accuracy of the interpolation scheme by one order of accuracy, M-AUSMPW+ combined with MLP-O4 and MLP-OS4 provides nearly the same accuracy as those of M-AUSMPW+ combined with MLP-5 and MLP-5S, respectively.

5.5. Sound generation by shock–vortex interaction

In addition to the numerical tests described above, the developed scheme is applied to the more realistic numerical simulation of sound generation by normal shock wave and vortex flow interactions. The generated sound in such interactions is relevant to a broadband shock-associated noise in imperfectly expanded jets and other flows such as impulsive noise produced by gun fire, explosion, engine exhaust and a mechanical impact process. The model problem of the interaction of an isolated vortex with a normal shock highlights the physical phenomena common to more complex flows. These phenomena have been calculated numerous times using various numerical techniques. For examples, an upwind second-order shock-capturing scheme, FCT scheme, ENO scheme, WENO scheme, sixth-order compact scheme and so on are used to study shock–vortex interaction [35,36,39–41].

In the present work, a normal shock wave with the Mach number $M_s = 1.29$ is propagating into a stationary vortex with the vortex Mach number $M_v = 0.39$, which is the same condition as in the experiment of Dosanjh and Weeks [34], where the vortex Mach number is defined by $M_v = u_\theta \mathrm{max}/c_\infty$ and $u_\theta \mathrm{max}$ is the maximum tangential velocity.

The Reynolds number in the experiment was 160,000. However, as is in Ref. [35], the present results are acquired in the inviscid Euler simulation because the numerical study of this paper is mainly focused on showing the effect of the vortex on the shock and the production of acoustic waves.

The initial vortex flow is assumed to have a swirling flow profile [35,36] with zero net circulation to produce an exponentially decaying induced velocity. Thus, the initial velocity distribution is as follows [42].

Tangential velocity:

$$u_\theta(r) = M_v \frac{r}{r_v} \exp\left[\frac{1-\varsigma^2}{2}\right]. \tag{5.7a}$$

Radial velocity:

$$u_r = 0. \tag{5.7b}$$

Vorticity distribution:

$$\omega(r) = M_v(2 - (r/r_v)^2) \exp\left[\frac{1-\varsigma^2}{2}\right], \tag{5.7c}$$

where the velocity is normalized by the speed of sound c_∞ upstream of the shock wave.

It is assumed that the flow is isentropic. Therefore, the initial distributions of the velocity, density and pressure are expressed by

$$u_0(x,y) = -M_v \frac{y}{r_v} \exp\left[\frac{1-\zeta^2}{2}\right], \tag{5.8}$$

$$v_0(x,y) = M_v \frac{x}{r_v} \exp\left[\frac{1-\zeta^2}{2}\right], \tag{5.9}$$

$$\rho_0(x,y) = \left[1 - \frac{\gamma-1}{2} M_v^2 \exp(1-\varsigma^2)\right]^{\frac{1}{\gamma-1}}, \tag{5.10}$$

$$p_0(x,y) = \frac{1}{\gamma}\left[1 - \frac{\gamma-1}{2} M_v^2 \exp(1-\varsigma^2)\right]^{\frac{\gamma}{\gamma-1}}, \tag{5.11}$$

where $\varsigma = \sqrt{(x-x_v)^2 + (y-y_v)^2}/r_v$ and r_v is the vortex core radius. In the above expression, the density and the pressure are normalized by ρ_∞ and the speed of sound c_∞, where the subscript ∞ denotes the flow quantity upstream of the shock wave. In this computation, the computational domain ranges from $(-20, -20)$ to $(5, 10)$. The number of grid points is 400 by 400 with the uniform grid spacing. Initially, the vortex core was located at the point of $(-5, -5)$ and the normal shock wave was located at $x = 5$. Then, 18 non-dimensional times evolved. M-AUSMPW+ combined with MLP-OS4 was applied for spatial discretization and the 3rd order TVD Runge–Kutta scheme with $\Delta t = 0.01$ was used for time integration.

In Fig. 20, the time development of the pressure field of the vortex interacting with the shock wave is presented. Here, the sound pressure Δp is defined as $\Delta p = (p - p_s)/p_s$ where p_s is the pressure behind the shock wave. And, the vortex rotates in the clockwise direction. In the figures, the solid line denotes the compression region ($\Delta p > 0$) and the dashed line denotes the rarefaction region ($\Delta p < 0$). The computational result clearly shows the basic structure of sound generation during the development of the interaction of vortex and shock waves. Fig. 20a shows the deformation of the initially planar shock wave and the generation of the compression region and the rarefaction region in the beginning of the shock–vortex interaction. In Fig. 20b, the generation of the precursor and its quadrupolar nature are seen clearly. As the interactions develop, the reflected shock waves, which are emanated from the incident shock wave, are observed in Fig. 20c. Because the sense of rotation of the vortex is clockwise, the strength and the propagation velocity of the shock wave that moves

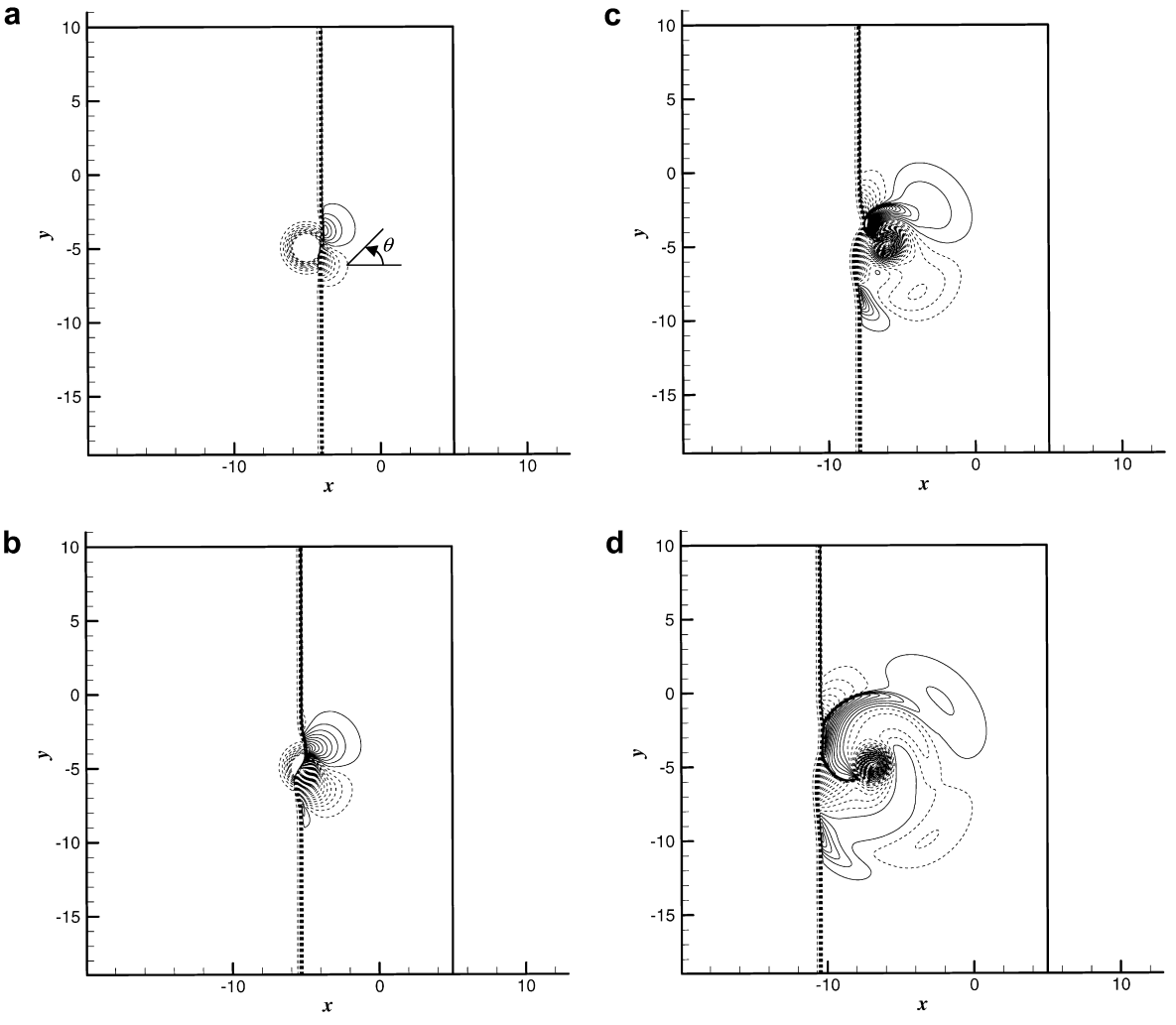

Fig. 20. Time development of the pressure field (Δp) at (a)$t = 9$, (b)$t = 10$, (c)$t = 12$, (d)$t = 14$. Hundred contour levels from −0.48 to 0.16.

upward, are larger than those of the shock wave that moves downward. Lastly, Fig. 20d shows the generation of a second sound which also has a quadrupolar nature.

Fig. 21 shows the sound pressure distributions for a fixed value of $\theta = 45°$ at $t = 14.2$, 15.2, 16.2 and 17.2, in agreement with the Navier–Stokes results of Inoue et al. It is clearly seen that both the precursor and the second sound propagate radially from the vortex core and their amplitudes are inversely proportional to the square root of the radial distance r from the vortex core. In Fig. 22, the circumferential distribution of Δp of the precursor and the second sound at $t = 16.2$ are plotted. In the present result, the radii of the precursor and the second sound are about 10.7 and 8.8, respectively. The radii of the precursor and the second sound are defined as the distance between the vortex core and the reflected shock waves at $\theta = 90°$, which are the same definitions used in Ref. [35 and 36]. Fig. 22 clearly shows the quadrupolar natures of the precursor and the second sound, and the anti-phasic variation of the second sound to the precursor.

For the detail comparison with the results of the Navier–Stokes simulation by Inoue et al., the isopycnics, isobars of the sound pressure, and the computational Schilieren picture are presented in Figs. 23a,

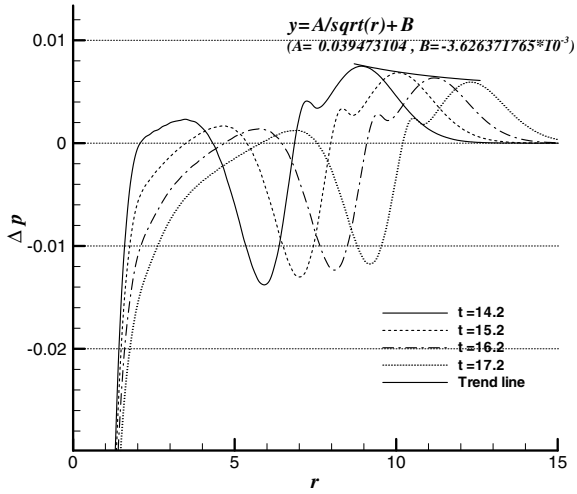

Fig. 21. Radial distributions of the sound pressure (Δp) at $\theta = 45°$.

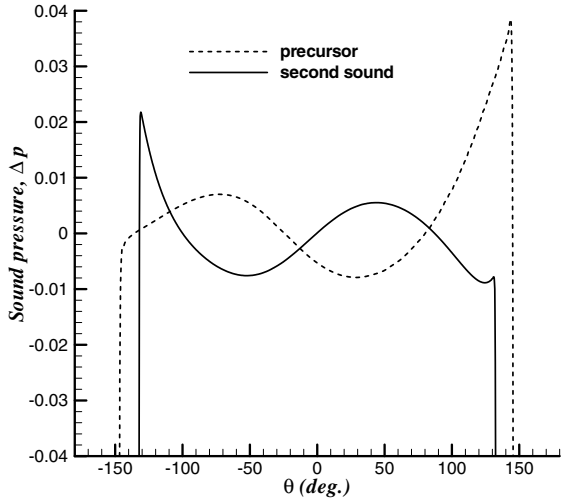

Fig. 22. Circumferential distributions of the sound pressure (Δp) at $t = 16.2$. The radii of the precursor and the second sound are 10.7 and 8.8, respectively.

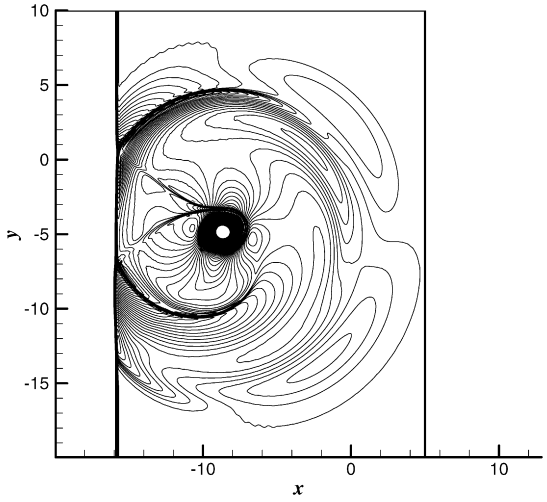

Fig. 23a. Isopycnics at $t = 16.2$. The contour levels are from 1.26 to 1.60 with an increment of 0.0029.

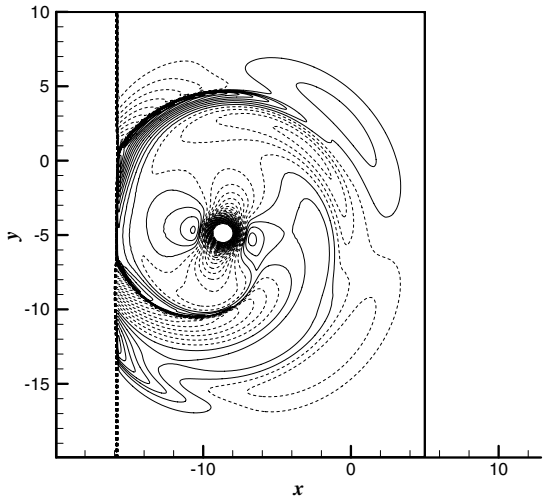

Fig. 23b. Isobars at $t = 16.2$. The contour levels are from -0.16 to 0.24 with an increment of 0.0033.

23b and 24, respectively. Although the grid system used in this test is coarser than that used in the Navier–Stokes simulation (The number of grid points of the Navier–Stokes simulation was 1044 by 1170. And, the stretched grid system, which has the grid spacing of $\Delta x = \Delta y = 0.0025$ near the shock wave, is used.), the present result shows good agreement with the Navier–Stokes simulation. The Mach reflection and two slip-lines that emanated from the triple points are clearly seen in the isopycnics of Fig. 23a. In addition, the sound pressure field in Fig. 23b and the Schilieren pictures are very similar to those of the Navier–Stokes simulation.

In Fig. 25, the circumferential distributions of the pressure amplitude, $(p_2 - p_p)/p_s$, are compared with the experimental result [34], the inviscid Euler result [35], the Navier–Stokes result [36] and the theoretical result [43]. Here, p_2 denotes the second sound pressure and p_s the pressure of the precursor. As seen from Fig. 25, the present result shows good agreement with the experimental result. Furthermore, it is found that the quantitative difference between the present result and the experimental result is almost same as that of the Navier–Stokes and previous inviscid Euler. As mentioned in Ref. [36], the quantitative difference between the present result and the experimental result are negligible with regard to the different flow patterns between the Schilieren pictures in the experiment and in the computations.

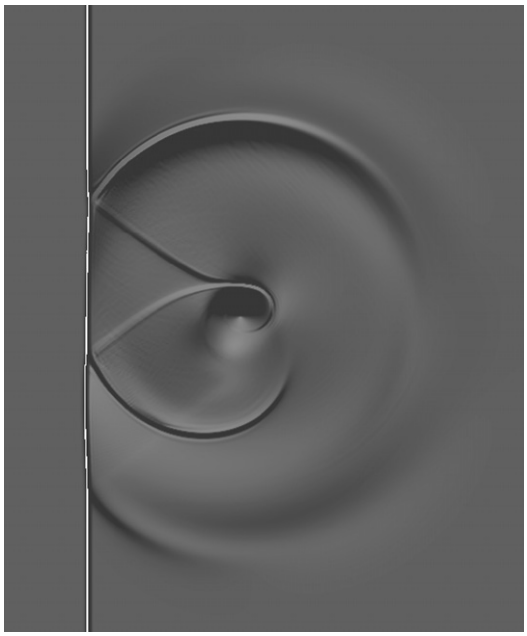

Fig. 24. Computational Schilieren pictures at $t = 16.2$.

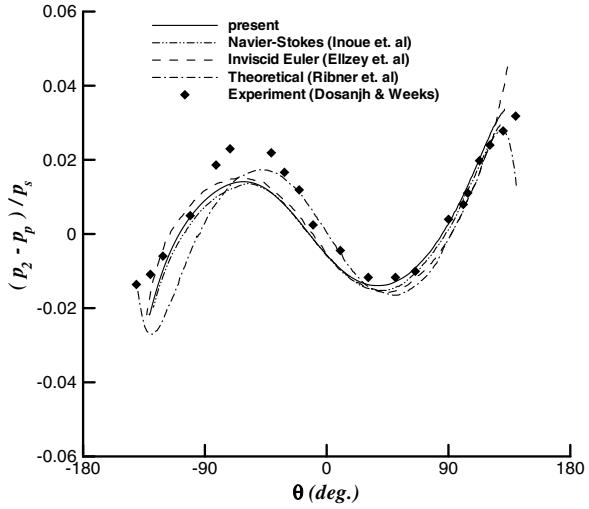

Fig. 25. Circumferential distributions of the pressure amplitude, $(p_2 - p_p)/p_s$.

In order to evaluate the capability of the developed scheme more clearly, the grid convergence test is performed. AUSMPW+ with MLP5 is chosen as the representative previous scheme, where the concept of regional distinction, smooth, rapidly varying and discontinuous regions is not applied. Fig. 26 is the comparison of density contours. Case (a)–(c) are the results obtained by AUSMPW+ combined with MLP5 on coarse (200 by 200), medium (282 by 282) and fine (400 by 400) grid systems, and cases (d)–(f) are results by M-AUSMPW+ combined with MLP-OS4 on the same grid systems. As in Fig. 26a and b, AUSMPW+ with MLP5 on the medium grid system provides more diffusive result than M-AUSMPW+ with MLP-OS4 on the coarse grid system, especially around the reflected shock waves and in the circle region. M-AUSMPW+ with MLP-OS4 on the medium grid system almost reaches the grid converged result, M-AUSMPW+ with

MLP-OS4 on the fine grid system. Figs. 27 and 28 show the more quantitative comparisons of density distribution along the line $x = -13.7$ and in the core region, respectively. As seen in Fig. 27, M-AUSMPW+ with MLP-OS4 captures the reflected shock wave more sharply than AUSMPW+ with MLP5. The density profile calculated by AUSMPW+ with MLP5 is somewhat smeared. Although the core pressure calculated by AUSMPW+ with MLP5 seems to be similar to that by M-AUSMPW+ with MLP-OS4 (see Fig. 28), it cannot describe the wave profile around the reflected shock waves because MLP limiter never admits local extrema like conventional TVD schemes. Overall, M-AUSMPW+ with MLP-OS4 gives about two times more accurate result than that of MLP5. Fig. 29 shows the decomposition of the computational domain into smooth, rapidly varying and discontinuous regions by the proposed distinguishing mechanism at three different shock positions. As shown in the figures, the developed distinguishing mechanism keeps the application of the

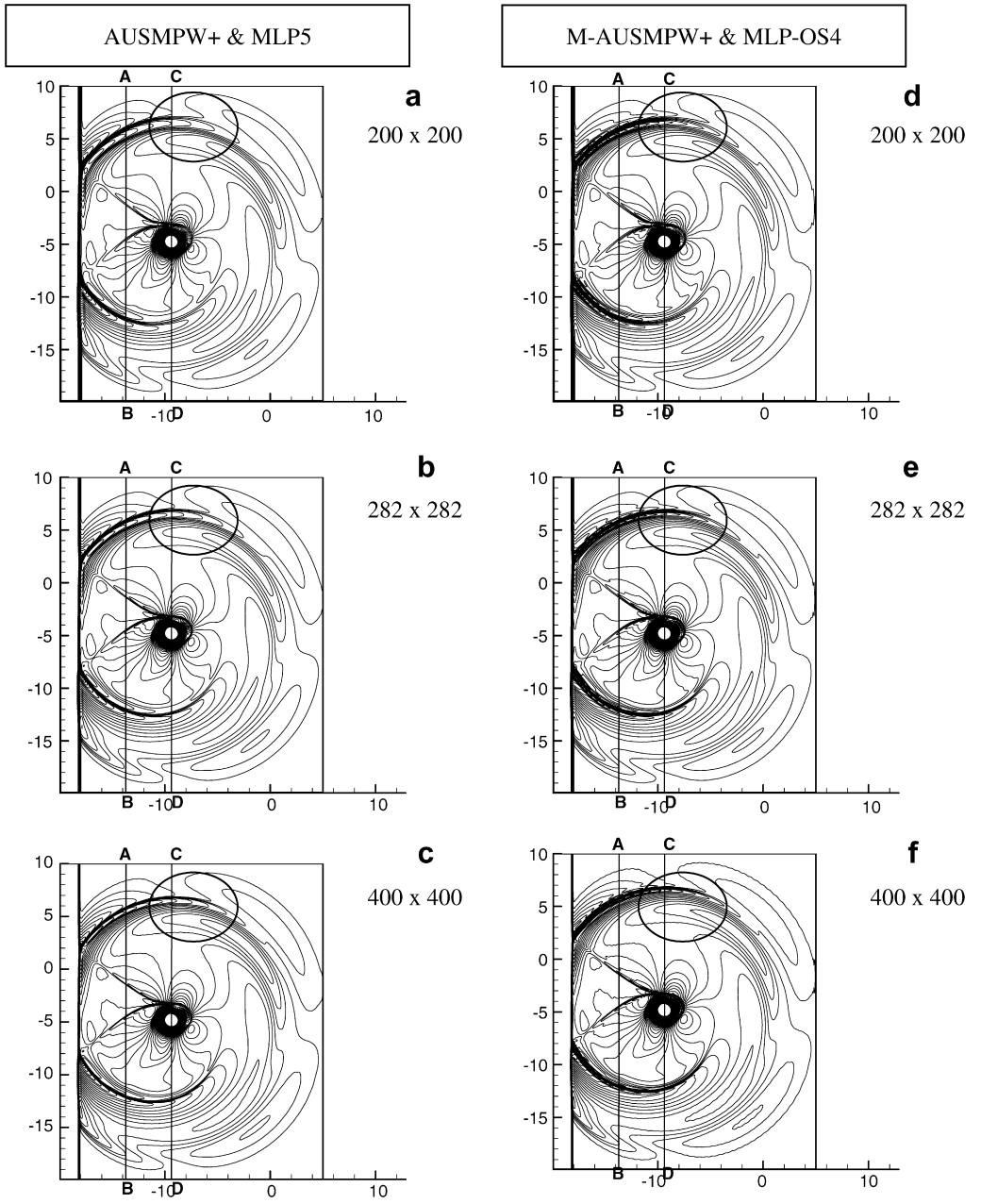

Fig. 26. Density distributions according to grid points and numerical schemes.

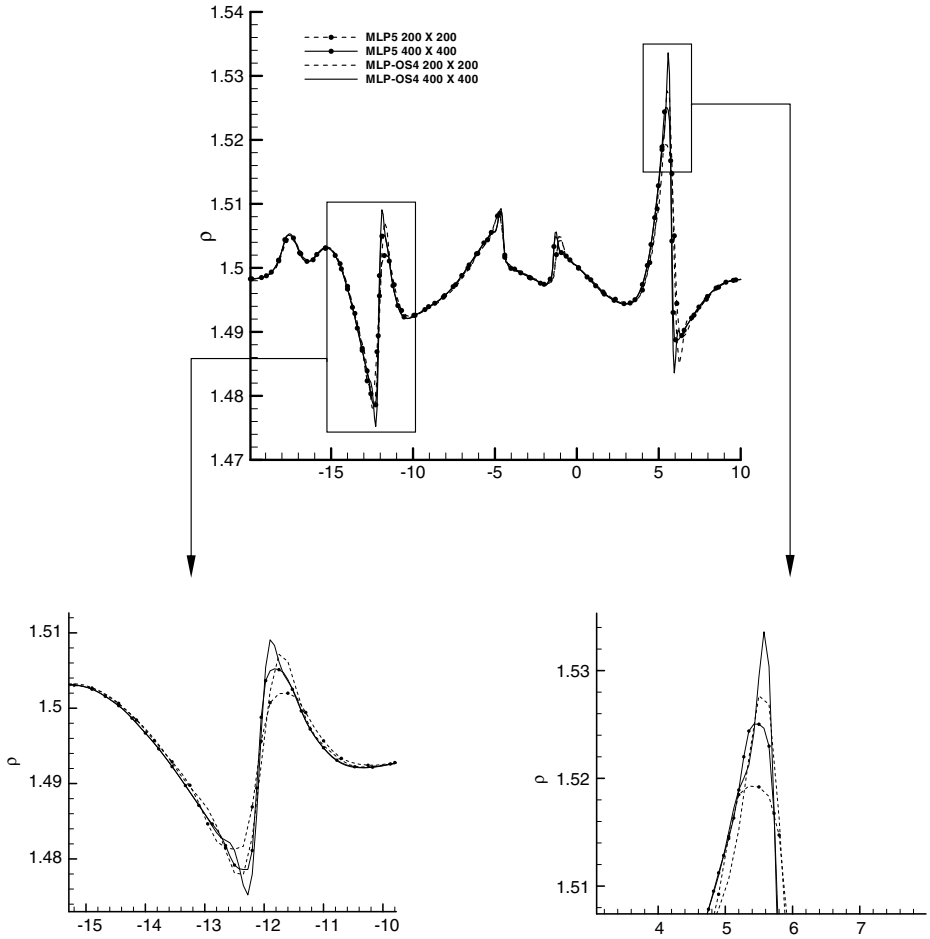

Fig. 27. Comparison of density distributions along line AB.

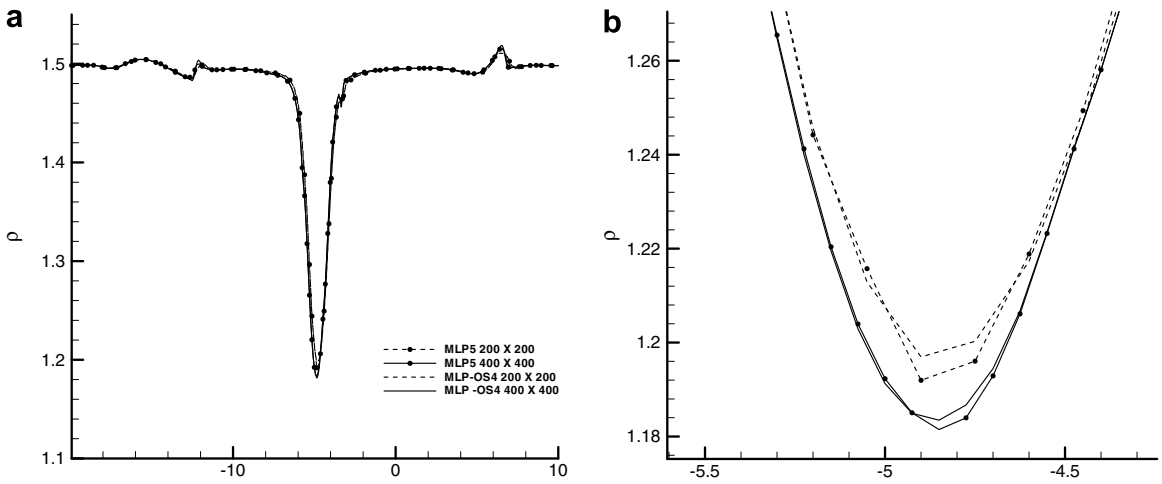

Fig. 28. Comparison of density distribution in core region (along line CD) (a) Vortex core. (b) Zoomed view.

limiting process bound around the shock. And, it can be inferred that this process helps M-AUSMPW+ with MLP-OS4 to give a reduction effect more than two times than that of the AUSMPW+ with MLP5, which is shown in Fig. 26.

5.6. Muzzle blast flow problem

The purpose of the muzzle blast flow simulation is to evaluate the applicability of the developed scheme to the more complicated mixture of various linear and nonlinear phenomena. The muzzle blast flow problem can be considered as an impulsive sound generation process. This impulsive sound commonly contains complicated physics, which consists of several nonlinear and linear phenomena such as bow shock, vortices, blast shock waves, projectile, shear layer and their interactions. Although several researches have been performed on the muzzle blast problem [44–46], the flow characteristics of muzzle blast and shooting noise generation mechanism have not been revealed clearly. Schmidt and Shear [46] have performed the optical measurements of blast waves and propellant gases. However, their experimental approaches had difficulties in discriminating between the flow structure and muzzle flash. The recent numerical study on the muzzle blast flow is performed by Jiang et al. [44,45]. In the study, numerical simulation was essentially based on the low-order numerical methods. Therefore, it was not sufficient to investigate the complex phenomena occurring in the muzzle blast flow.

For a convenient comparison with the conventional approach, the present numerical procedure is based on that of Ref. [44]. It is composed of the two computational steps. The first step is the calculation of precursor wave with the exit condition of the shock tube, and the second one is the calculation of the moving projectile under the initial condition which is the shock tube solution at the first step. In the first step, the precursor wave is generated by the gases in front of the projectile. It is assumed that the propellant gas velocity at the exit of the shock tube is equal to the launching speed of the projectile, which was confirmed in the previous research of Schmidt et al. [46]. To investigate the influence of the drag and friction in discharging process from shock tube, the flow conditions behind the projectile are obtained from Ref. [44]. According to this consideration, the exit condition of the shock tube can be calculated by using the Poisson's adiabatic equation.

Finally, the exit condition of the shock tube is obtained as follows:

gas speed of propellant gas: $M_e = 1.25$,
ratio of the pressure behind the shock: $p_e/p_\infty = 4.5$,
ratio of the density behind the shock: $\rho_e/\rho_\infty = 2.667$.

The surrounding conditions outside of the shock tube are assumed to be ambient conditions.

The second step is performed after the first step solution is obtained. The initial flow field of the second step calculation is imposed from the first step solution. In this calculation, the projectile is assumed as a cylindrical body, which is appropriate to observe the generation mechanism of blast waves.

The governing equations for the computation are axisymmetric Euler equations. The computation domain uses 700 by 300 grid points with a uniform grid spacing, $\Delta x = \Delta y = 0.025$. The diameter of the projectile is 1 and the thickness of the shock tube wall is 0.5, which is non-dimensionalized by the diameter of the projectile. The shock tube length is assumed to be identical to the projectile length. The axisymmetric boundary condition is applied along the shock tube axis, whereas the other far boundary conditions are the nonreflecting boundary conditions. For the last part of the domain, which is the shock tube wall, the slip boundary condition is applied. In addition, a moving boundary condition is implemented to describe the supersonic projectile, whose speed is $M_p = 1.25$.

Fig. 30 shows the density distributions at non-dimensionalized times of 100, 220, 340, 460, 580 and 700, respectively. As the projectile is discharged from the shock tube, the flow is compressed and the primary blast wave is generated. In Fig. 30(a), the generations of the primary blast wave, precursor shock wave, vortex ring and mach disk are presented. After the projectile moves out, secondary blast wave generation can be observed, as shown in Fig. 30(b). Successively, Fig. 30(c) shows the development of the bow shock in front of the supersonic moving projectile. After that, as the projectile moves farther, several complex vortices are generated (Fig. 30(d)–(f)) due to the interactions among the shock and projectile or shear layer and shock, jet and shock, and so on.

The muzzle blast flow-field is generally characterized by two blast waves, a shock wave and moving projectile interactions. In Fig. 30, the basic structures of the muzzle blast flow including the generations and deformations of the primary blast wave, precursor shock and the secondary blast wave are observed with respect to

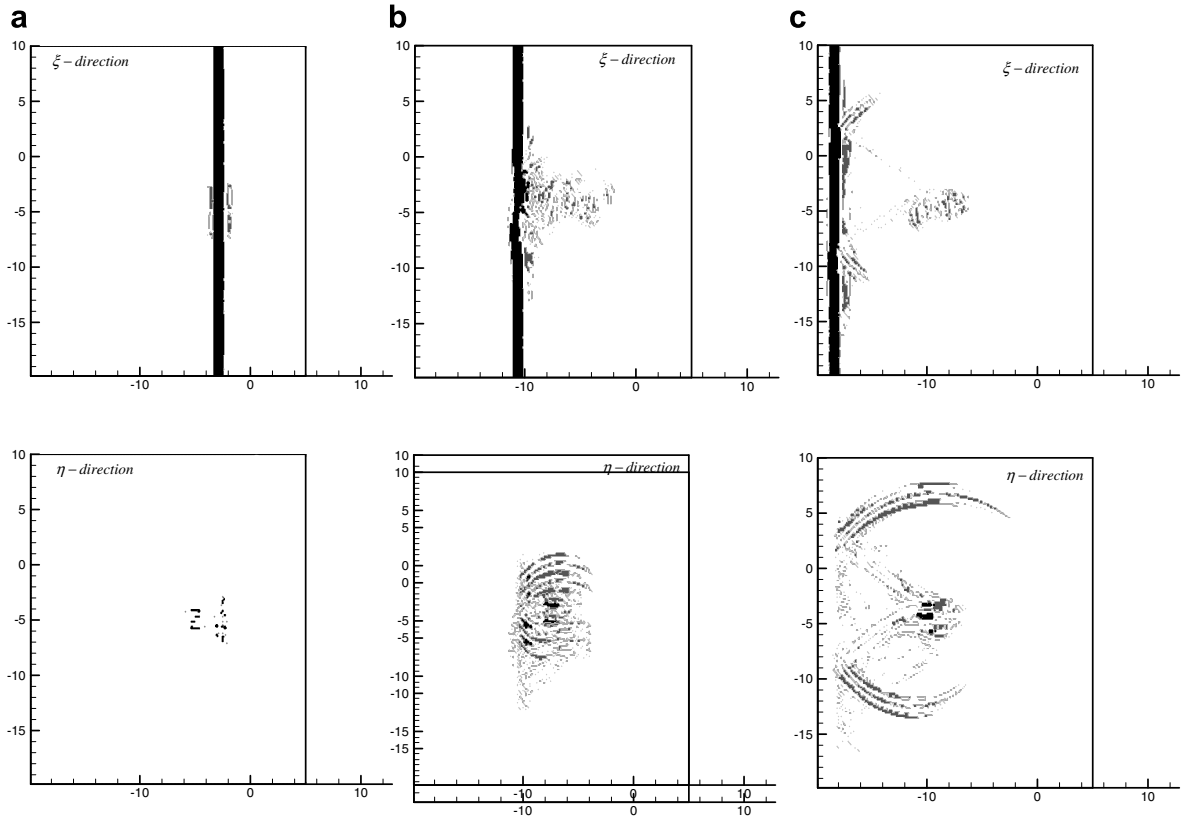

Fig. 29. Illustrations of the regional distinction by the distinguishing mechanism at (a) $t = 6$, (b) $t = 12$, (c) $t = 18$. (■: discontinuity, ■: rapidly varying region, □: continuous region).

time. Considering the complexity of a muzzle blast flow-field and the complicated nonlinear phenomena in the flow-field, it is inferred that the developed method can broaden the application area of CAA to complex nonlinear physics.

6. Concluding remarks

New treatments for the high-order finite volume scheme for the CAA applications were developed to reduce the numerical dispersion error substantially in the smooth region while monotonic profiles were yielded in the discontinuous region. The distinguishing mechanism between continuous and discontinuous regions, which is based on the Gibbs phenomena in computation, is introduced to improve the solution accuracy in the continuous region by restricting the application of MLP only in the discontinuous region. In addition, the wavenumber-extended optimization procedure based on the conservative requirement was newly proposed for the enhancement of the dispersion characteristic to capture the acoustic portion of the solution in the smooth region.

Through numerous test cases such as spherical wave propagation, nonlinear wave propagation, shock tube problem, double shock reflection, vortex preservation test, shock–vortex interaction and muzzle blast flow, the proposed scheme was verified to provide better resolution properties in the wavenumber space than the standard high-order finite volume schemes while yielding similar monotonicity in discontinuity to the original high-order MLP. In addition, it was shown that the developed method generally provided about two times accuracy improvement in terms of grid points than that of AUSMPW+ with MLP5, which provided about the standard 5th order spatial accuracy. Another desirable characteristic of the developed scheme was that

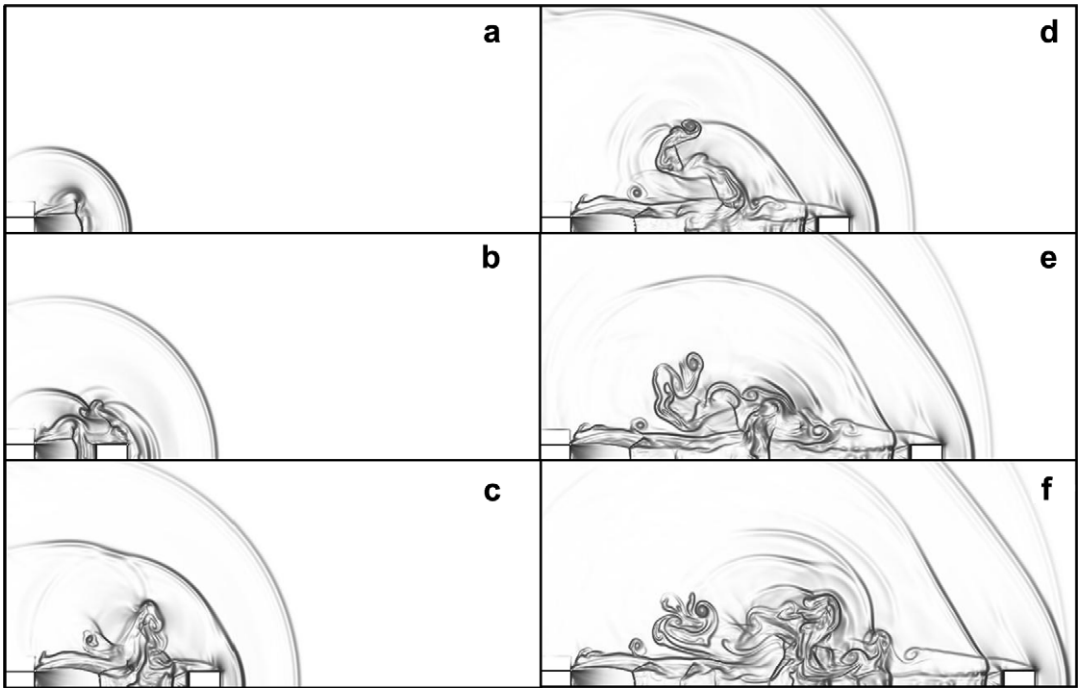

Fig. 30. Density distributions of muzzle blast flow at (a) $t = 100$, (b) $t = 220$, (c) $t = 340$, (d) $t = 460$, (e) $t = 580$, (f) $t = 700$.

it retained the advantages of the finite volume scheme as it minimized the numerical dispersion and dissipation errors and that it can be easily implemented to existing high-order finite volume solvers.

As a consequence, it was confirmed that the developed scheme can be a good candidate for the nonlinear CAA related with shock or discontinuity and its interaction with the sound field that it generates.

Acknowledgment

This work was supported by Grant Nos. R01-2006-000-10034-0 and R01-2006-000-10301-0 from the Basic Research Program of the Korea Science and Engineering Foundation.

References

[1] C.K.W. Tam, Computational aeroacoustics: issues and methods, AIAA Journal 33 (10) (1995) 1788.
[2] C.K.W. Tam, Computational aeroacoustics: an overview of computational challenges and application, International Journal of Computational Fluid Dynamics 18 (6) (2004) 547.
[3] T. Colonius, S.K. Lele, Computational aeroacoustics: progress on nonlinear problems of sound generation, Progress in Aerospace Sciences 40 (2004) 345.
[4] M. Wang, J.B. Freund, S.K. Lele, Computational prediction of flow-generated sound, Annual Review of Fluid Mechanics 38 (2006) 483.
[5] T. Colonius, S.K. Lele, Computational aeroacoustics: progress on nonlinear problems of sound generation, Progress in Aerospace Sciences 40 (2004) 345.
[6] C.K.W. Tam, J.C. Webb, Dispersion–relation-preserving finite difference schemes for computational acoustics, Journal of Computational Physics 107 (1993) 262.
[7] Y. Li, Wavenumber-extended high-order upwind-biased finite-difference schemes for convective scalar transport, Journal of Computational Physics 133 (1997) 235.
[8] D. Gaitonde, J.S. Shang, Optimized compact-difference-based finite volume schemes for linear wave phenomena, Journal of Computational Physics 138 (1997) 617.
[9] Y. Liu, Fourier Analysis of numerical algorithms for the Maxwell equations, Journal of Computational Physics 124 (1996) 396.
[10] V.G. Weirs, G.V. Candler, Optimization of weighted ENO schemes for DNS of compressible turbulence Technical Paper 97-1940 (AIAA Press, Washington, DC, 1997).

[11] C.K.W. Tam, J.C. Webb, A study of the short wave components in computational acoustics, Journal of Computational Physics 107 (2) (1993) 262.
[12] J.W. Kim, D.J. Lee, Optimized compact finite difference schemes with maximum resolution, AIAA Journal 34 (5) (1996) 887.
[13] M. Zhuang, R.F. Chen, Optimized upwind dispersion-relation-preserving finite difference schemes for computational aeroacoustics, AIAA Journal 36 (1998) 2146.
[14] M. Zhuang, R.F. Chen, Applications of the optimized upwind dispersion relation preserving schemes for multi-dimensional acoustic problems, Technical Paper 98-2367 (AIAA Press, Washington, DC, 1998).
[15] D.P. Lockard, K.S. Brentner, H.L. Atkins, High-accuracy algorithms for computational aeroacoustics, AIAA Journal 33 (1995) 246.
[16] A. Harten, High resolution schemes for hyperbolic conservation laws, Journal of Computational Physics 49 (3) (1983) 357.
[17] P.K. Sweby, High resolution schemes using flux limiters for hyperbolic conservation laws, SIAM Journal on Numerical Analysis 21 (5) (1984) 995.
[18] A. Harten, B. Enquist, S. Osher, S.R. Chakravarthy, Uniformly high order accurate essentially non-oscillatory schemes, III, Journal of Computational Physics 71 (2) (1987) 231.
[19] C.W. Shu, TVB uniformly high-order schemes for conservation laws, Mathematics of Computation 49 (179) (1987) 105.
[20] X-D. Liu, S. Osher, T. Chan, Weighted essentially non-oscillatory schemes, Journal of Computational Physics 115 (1994) 200.
[21] K.H. Kim, C. Kim, Accurate, efficient and monotonic numerical methods for multi-dimensional compressible flows Part II: multi-dimensional limiting process, Journal of Computational Physics 208 (2005) 570.
[22] K.H. Kim, C. Kim, Accurate, efficient and monotonic numerical methods for multi-dimensional compressible flows Part I: spatial discretization, Journal of Computational Physics 208 (2005) 527.
[23] J.C. Hardin, J.R. Ristorcelli, C.K.W. Tam, in: Proceedings of the ICASE/LaRC workshop on benchmark problems in computational aeroacoustics (CAA), CP-3300, NASA, 1995.
[24] D.V. Nance, K. Viswanathan, L.N. Sankar, Low-dispersion finite volume scheme for aeroacoustic applications, AIAA Journal 35 (2) (1997) 246.
[25] C.-W. Shu, Essentially non-oscillatory and weighted essentially non-oscillatory schemes for hyperbolic conservation laws, NASA/CR-97-206253 (NASA Langley Research Center, Hampton, VA, 1997).
[26] A.S. Lyrintzis, Review: The use of Kirchhoff's method in computational aero- and hydrodynamics, Journal of Fluids Engineering 116 (1994) 665.
[27] Z.J. Wang, R.F. Chen, Optimized weighted essentially nonoscillatory schemes for linear waves with discontinuity, Journal of Computational Physics 174 (2001) 381.
[28] C.K.W. Tam, Numerical Methods in Computational Aeroacoustics, AIAA Short Course, AIAA Press, Washington, DC, 1997.
[29] D. Gottlieb, C.-W. Shu, The Gibbs phenomenon and its resolution, SIAM Review 39 (1997) 644.
[30] T.W. Körner, Fourier Analysis, Cambridge University Press, 1989.
[31] P.M. Morse, H. Feshback, Methods of Theoretical Physics, McGraw-Hill, New York, 1953.
[32] J.N. Libii, Gibbs phenomenon and its applications in science and engineering, in: Proceedings of the 2005 American Society for Engineering Education Annual Conference and Exposition, Portland, Oregon, June, 2005.
[33] C.W. Shu, S. Osher, Efficient implementation of essentially non-oscillatory shock-capturing schemes, Journal of Computational Physics 77 (1988) 439.
[34] D.S. Dosanjh, T.M. Weeks, Interaction of a starting vortex as well as a vortex street with a traveling shock wave, AIAA Journal 3 (1965) 216.
[35] J.L. Ellzey, M.R. Henneke, J.M. Picone, E.S. Oran, The interaction of a shock with a vortex: shock distortion and the production of acoustic waves, Physics of Fluids 7 (1995) 172.
[36] O. Inoue, Y. Hattori, Sound generation by shock–vortex interactions, Journal of Fluid Mechanics 380 (1999) 81.
[37] C.K.W. Tam, H. Shen, K.A. Kurbatskii, L. Auriault, Z. Dong, J.C. Webb, Solutions of the benchmark problems by the dispersion-relation-preserving scheme, in: Proceedings of the ICASE/LaRC workshop on benchmark problems in computational aeroacoustics (CAA), Hampton, VA, October, 1994.
[38] G.B. Whitham, Linear and Nonlinear Waves, Wiley-Interscience, New York, 1974.
[39] K.R. Meadows, A. Kumar, M.Y. Hussaini, Computational study on the interaction between a vortex and a shock wave, AIAA Journal 29 (1991) 174.
[40] K.R. Meadows and D.A. Caughey, The role of shock motion and deformation in the generation of shock noise, AIAA Paper 96-1777 (1996).
[41] F. Grasso, S. Pirozzoli, Shock-wave-vortex interactions: shock and vortex deformations and sound production, Theoretical Computational Fluid Dynamics 13 (6) (2000) 421.
[42] G.I. Taylor, On the dissipation of eddies, The Scientific Papers of Sir Geoffrey Ingram Taylor, vol. 2, Cambridge University Press, Cambridge, UK, 1958, pp. 96–101.
[43] H.S. Ribner, Cylindrical sound wave generated by shock–vortex interaction, AIAA Journal 23 (1985) 1708.
[44] Z. Jiang, K. Takayama, B.W. Skews, Numerical study on blast flowfields induced by supersonic projectiles discharged from shock tubes, Physics of Fluids 10 (1998) 277.
[45] Z. Jiang, Wave dynamics processes induced by a supersonic projectile discharging from a shock tube, Physics of Fluids 15 (2003) 1665.
[46] E. Schmidt, D. Shear, Optical measurement of muzzle blast, AIAA Journal 13 (1975) 1048.